GEOTECHNICAL EXTREME EVENTS RECONNAISSANCE (GEER) ASSOCIATION

Turning Disaster into Knowledge

GEOTECHNICAL ASPECTS OF APRIL 1, 2014, M8.2 IQUIQUE, CHILE EARTHQUAKE

Report of the NSF Sponsored GEER Association Team

Editors and Lead Authors:
Kyle Rollins, Prof., Brigham Young University
Christian Ledezma, Asst. Prof., Pontificia Universidad Catolica de Chile,
Gonzalo Montalva, Asst. Prof., Universidad de Concepción

Contributing Authors:
Alix Becerra, Graduate Student, Pontificia Universidad Católica de Chile, Gabriel Candia, Professor, Universidad del Desarrollo; Darío Jara, Graduate. Student, Universidad de Concepción. Kevin Franke, Asst. Prof., Brigham Young University; Christian Ledezma, Asst. Prof., Pontificia Universidad Catolica de Chile, Kyle Rollins, Prof., Brigham Young University, Esteban Saez, Asst. Prof., Pontificia Universidad Catolica de Chile

GEER Association Report No. GEER-038

Version 1.2: October 22, 2014

Acknowledgments

The work of the GEER Association is based upon work supported in part by the National Science Foundation through the Geotechnical Engineering Program under Grant No. CMMI-0825734. Any opinions, findings, and conclusions or recommendations expressed in this material are those of the authors and do not necessarily reflect the views of the NSF. The GEER Association is made possible by the vision and support of the NSF Geotechnical Engineering Program Directors: Dr. Richard Fragaszy and the late Dr. Cliff Astill. GEER members also donate their time, talent, and resources to collect time-sensitive field observations of the effects of extreme events.

Special acknowledgment is given to the Chilean National Commission for Scientific and Technological Research (CONICYT) under FONDAP Award Number 15110017 (National Research Center for Integrated Natural Disaster Management, CIGIDEN Project), FONDEF Award Number D1011027 (FONDEF MAS ANDES Project), Fondecyt de Iniciacion Award Number 11121404, and the Civil Engineering Department of Universidad de Concepcion.

Table of Contents

1. Seismological background and recorded ground motions

The Mw 8.2 event on April 1, 2014 was triggered at 20:46:45 local time, with hypocentral location 19.572°S, 70.908°W, and 38.9 km deep, as reported by the Chilean National Seismological Center (CSN). The main seismological setting is given by the large seismic gap from the 1877 Mw 8.8 event (see Fig. 1.1), a swarm that took place on the rupture plane two weeks prior to the main event, and a Mw 7.6 aftershock that might have caused more damage than the main event (according to residents' testimonies).

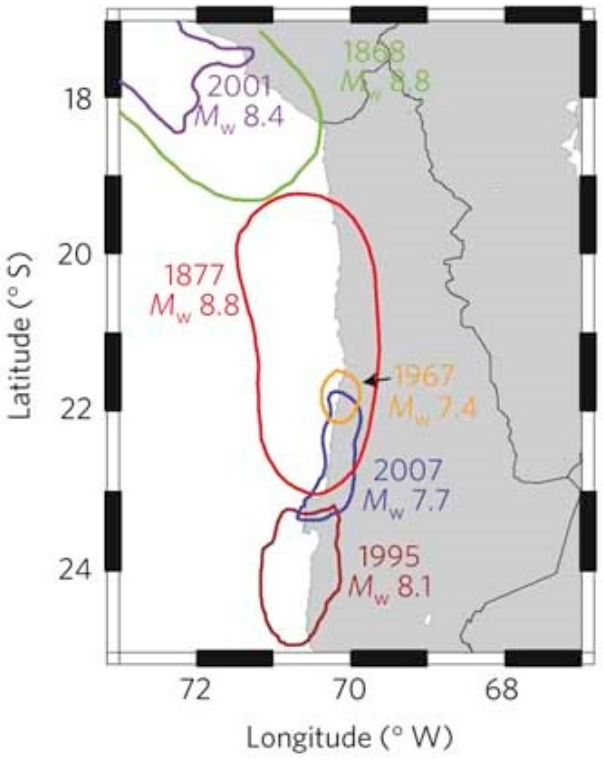

Fig. 1.1. Northern Chile's seismic gap (Contreras et al., 2012)

Foreshocks

Before the main event an earthquake swarm occurred in the same area located on the same plane of the main event´s rupture (Barrientos, 2014). These events had a maximum magnitude of Mw 6.7 on March 16th, which triggered a tsunami warning evacuation in the city of Iquique and led to speculation on the predictability of megathrust events (Brodsky and Lay, 2014). This foreshock activity evolved towards the hypocentral zone, and had a maximum recorded acceleration of 5.5% of g at station TA01 (see Fig. 1.5). Fig. 1.2 shows the record for this station.

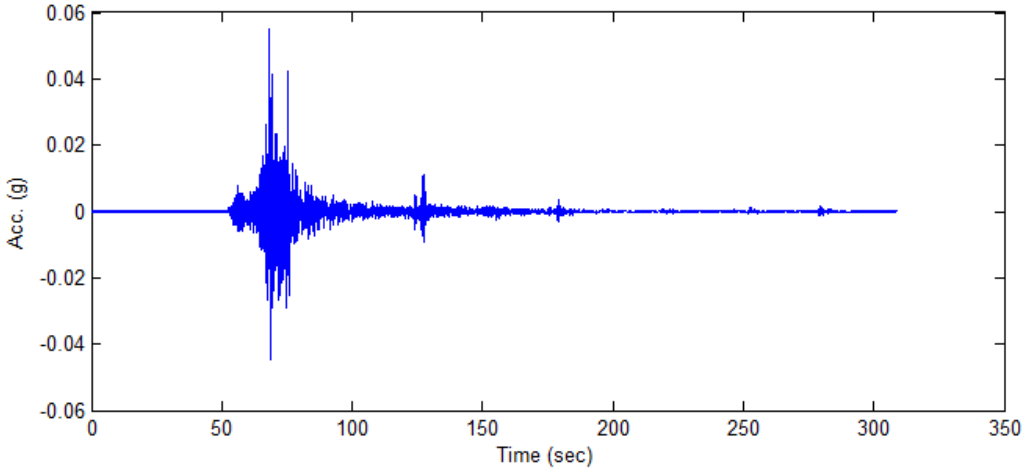

Fig. 1.2. Acceleration record of the main foreshock on March 16th 2014. North-south component of station TA01.

Main Event

The main event, as most of these large events do, has many solutions for the rupture plane. According to the USGS (Hayes, 2014) the rupture plane's most significant slip, and thus energy release, occurred 34 km to the northwest of Iquique, the city with the most severe damage. The rupture area had a width and length of about 240 and 270 km respectively, with a maximum slip on the order of 8 m. Fig. 1.3 shows the finite fault solution.

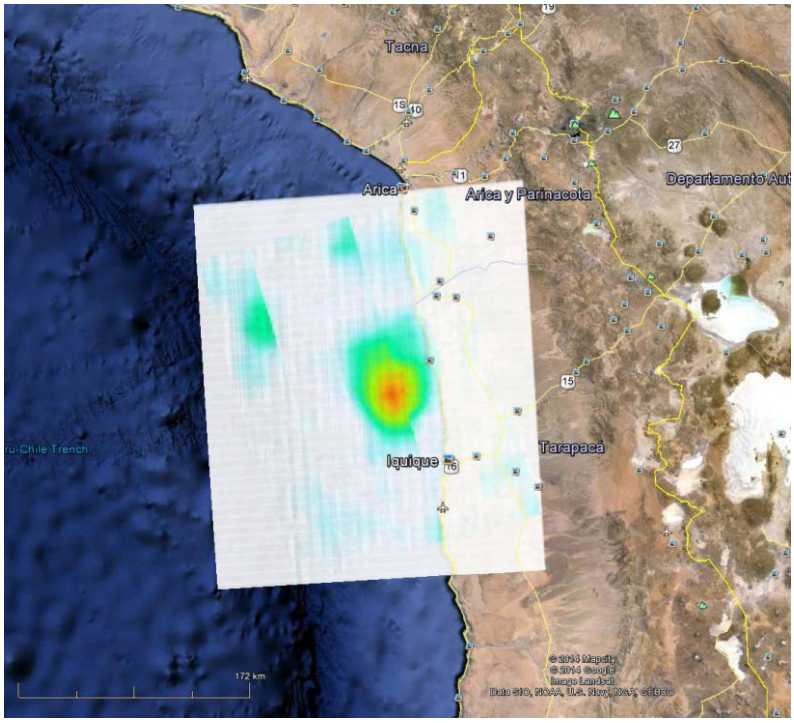

Fig. 1.3. Finite fault solution of the main event according to the USGS (Hayes, 2014).

Aftershock

The Mw 7.6 aftershock on April 3, 2014 was felt in the entire affected region, and according to many of the residents, much of the damage was observed after this shock rather than after the main event. The currently available ground motion records for this event reached PGA values over 21% g. Fig. 1.4 shows an example of the recorded motions of this event.

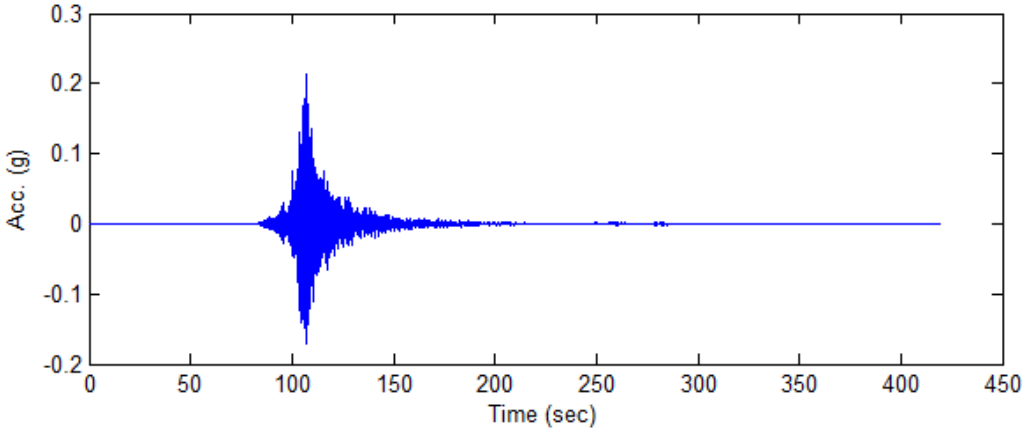

Fig. 1.4. Aftershock ground motion for the NS component at PB11.

Recorded Ground Motions

Available ground motions total more than 20 digital recordings of accelerometer stations. In addition, there are a number of broadband stations that also recorded the event, some of them were saturated in the near field. In terms of available ground motion records, the Iquique 2014 earthquake is the best ever recorded in Chile. Pre-event noise is available to perform signal correction as required by different scientists, the seismic swarm, as well as the aftershock, were also recorded by many of these stations.

Figs. 1.5 and 1.6 show the locations for the available ground motion stations near the rupture plane. A close-up view of the stations that recorded the main shock in the city of Iquique and Alto Hospicio is shown in Fig. 1.6, as much of this report will address observed features at these locations.

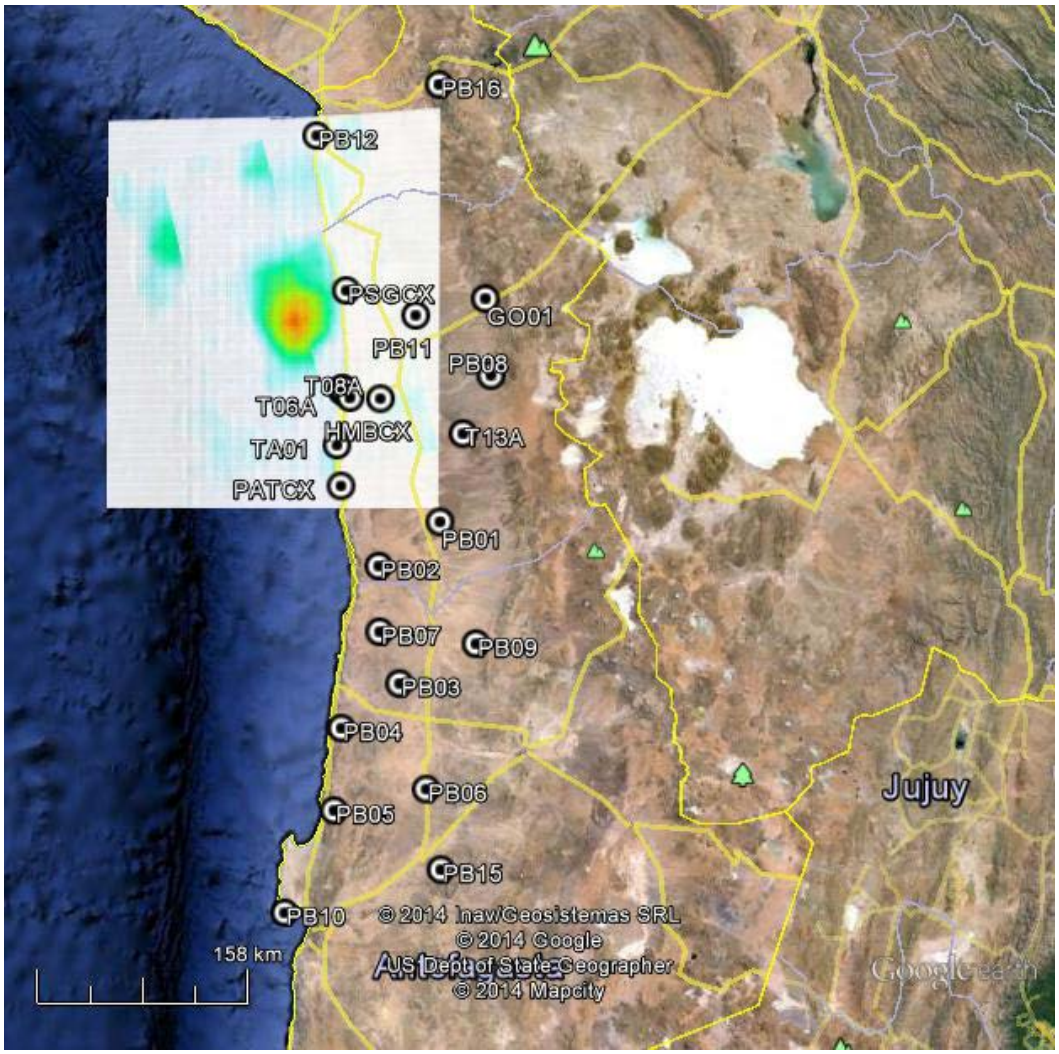

Fig. 1.5. Ground motion station locations ranging from the north of Arica to Antofagasta.

Fig. 1.6. Ground motion stations in the area of Iquique and Alto Hospicio.

Figs. 1.7 and 1.8 show the recorded accelerograms for 16 of the stations in the direction of maximum acceleration: north-south (NS).

Observed spectral ordinates were compared against those predicted by a recent ground motion prediction equation (BCHydro, Abrahamson et al., 2014). Fig. 1.9 through 1.12 show the comparison for PGA, and S_a at periods of 0.3, 1.0 and 3.0 seconds. The shear-wave velocity values for the V_{s30} computation were obtained from Podesta (2014).

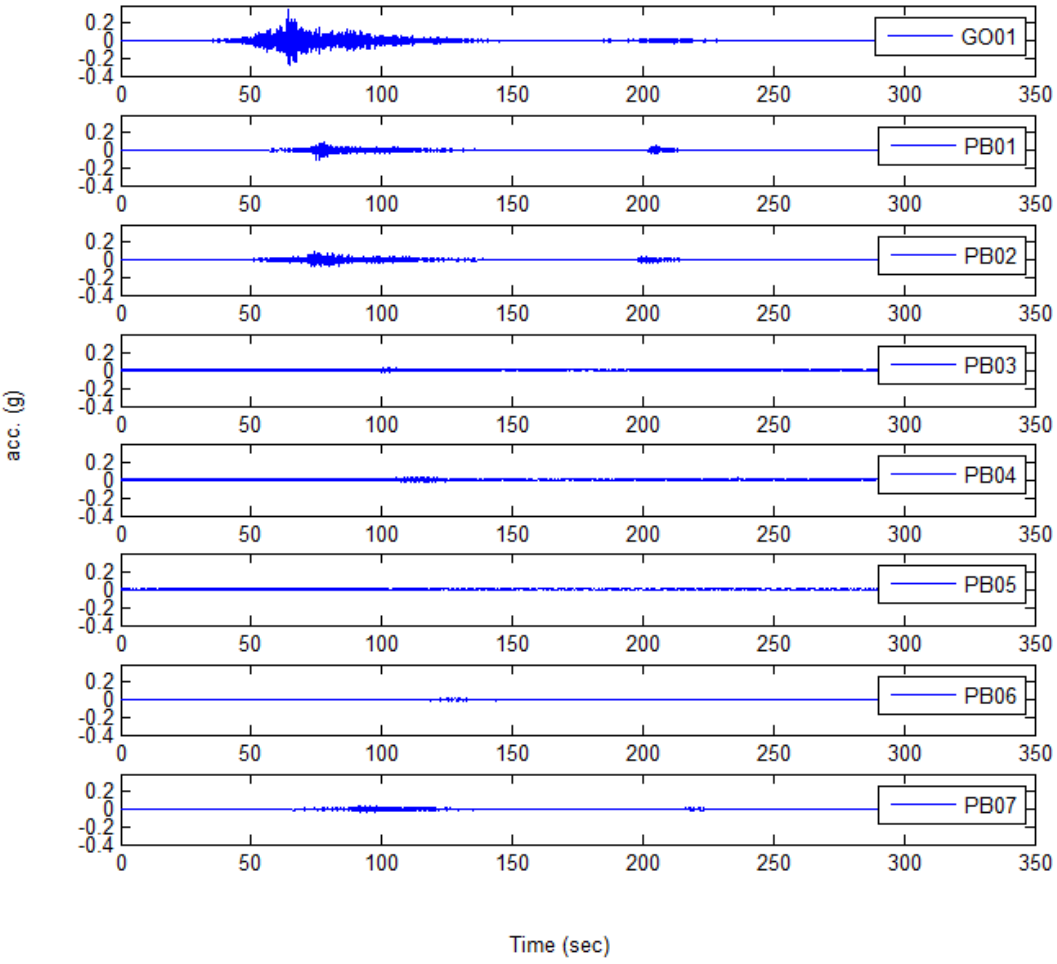

Fig. 1.7. Recorded acceleration ground motions for the NS component of stations GO01 to PB07. Records available from www.sismologia.cl (under "informes")

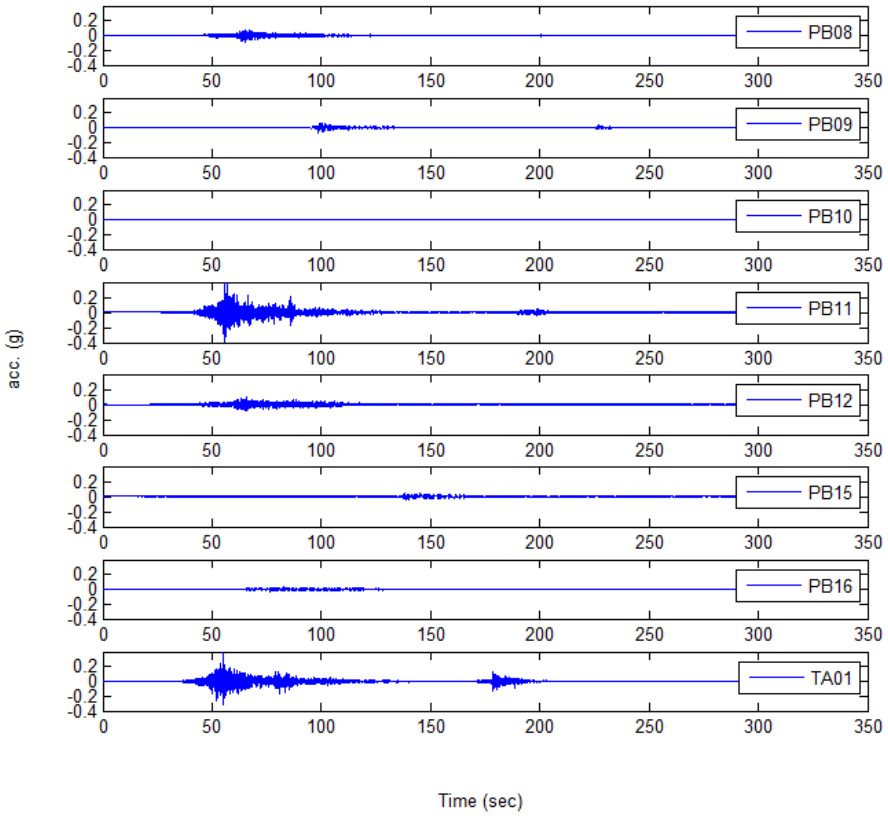

Fig. 1.8. Recorded acceleration ground motions for the NS component of stations PB08 to TA01. Records available from www.sismologia.cl (under "informes").

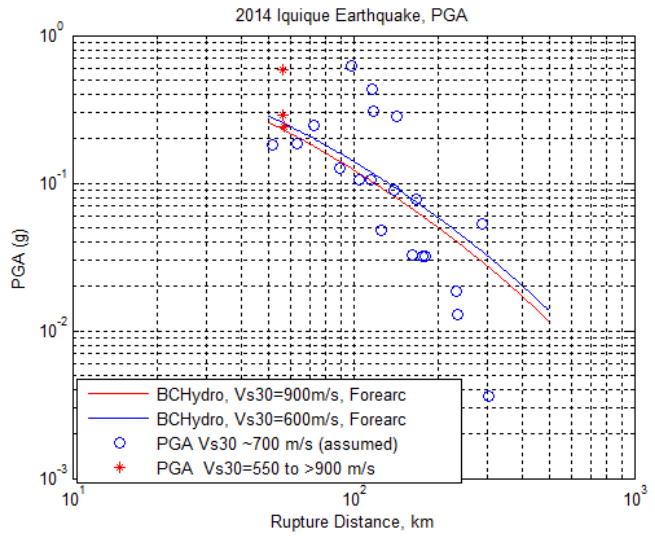

Fig. 1.9. Observed versus predicted PGA values. Red icons correspond to ground motion stations in Iquique with good constraint on V_{s30}, while blue circles are ground motion stations mainly on the desert with hard soil conditions expected to have V_{s30} higher than 700 m/s.

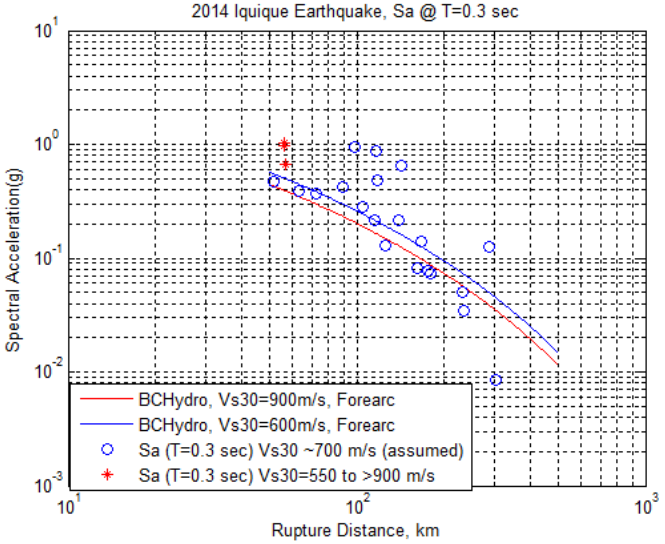

Fig. 1.10. Observed versus predicted Sa values for a period of 0.3 seconds. Red icons are ground motion stations in Iquique with good constraint on V_{s30}, while blue circles are ground motion stations mainly on the desert with hard soil conditions expected to have V_{s30} higher than 700 m/s.

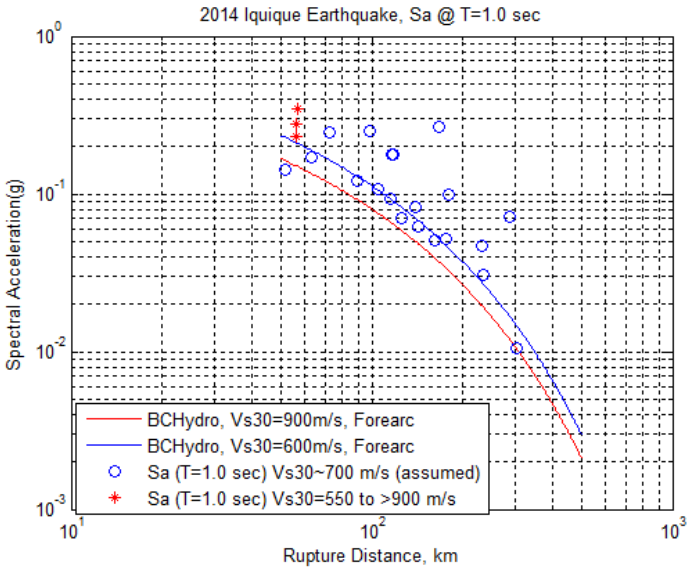

Fig. 1.11. Observed versus predicted Sa values for a period of 1.0 second. Red icons are ground motion stations in Iquique with good constraint on V_{s30}, while blue circles are ground motion stations mainly on the desert with hard soil conditions expected to have V_{s30} higher than 700 m/s.

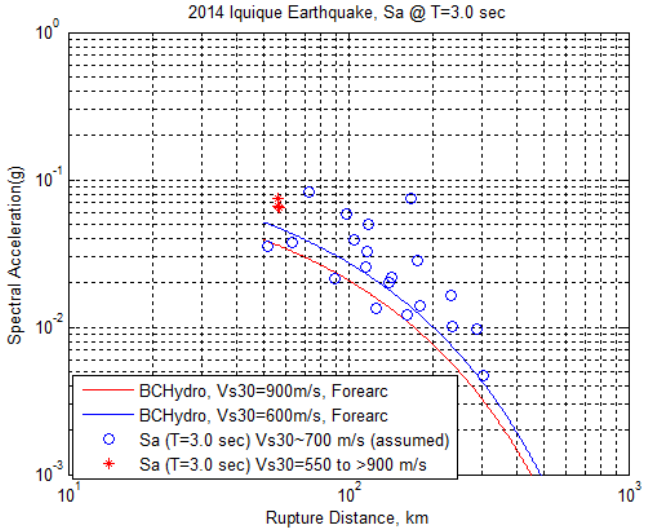

Fig. 1.12. Observed versus predicted Sa values for a period of 3.0 seconds. Red icons are ground motion stations in Iquique with good constraint on V_{s30}, while blue circles are ground motion stations mainly on the desert with hard soil conditions expected to have V_{s30} higher than 700 m/s.

Comparison with local standard

The Chilean standard for earthquake resistant design of buildings (NCh 433) showed a reasonable agreement with the large intensities registered at four stations shown in fig. 1.13. However, station T03A, located right in front Cavancha beach and nearby high-rise buildings has a spectrum that exceeded the code values for frequencies higher than 3 Hz. The code spectra shown here do not consider any ductility (i.e. R factors) and are computed for Iquique's seismic zone.

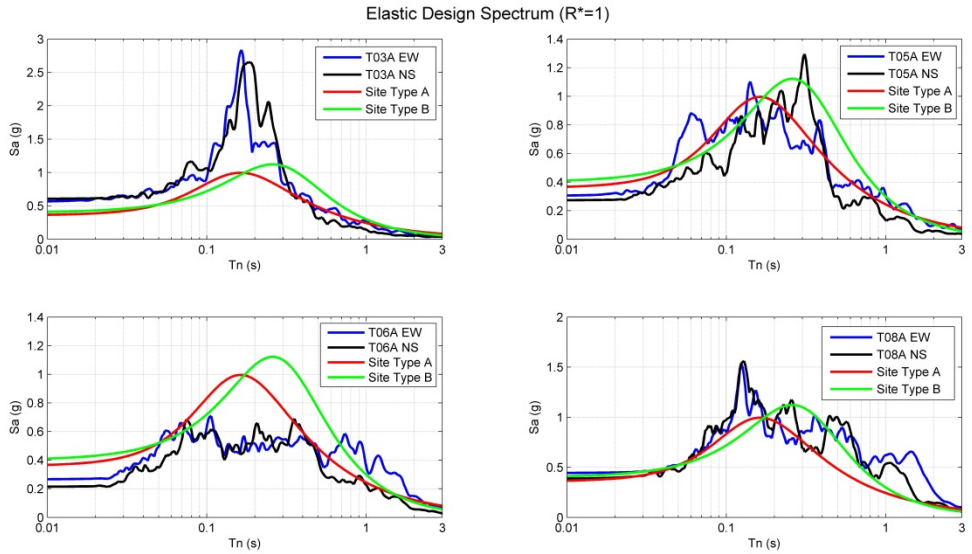

Fig. 1.13. Elastic response spectra of the measured motions at three stations in Iquique (T03A, T05A, and T06A) and one at Alto Hospicio (T08A) versus Chilean code elastic spectra.

References

Abrahamson, N., N. Gregor, and K. Addo (2014). unpublished report, 2014

Abrahamson, N., Gregor, N., Addo, K. (2014). BCHydro ground motion prediction equations for subduction earthquakes, Earthquake Spectra, submitted.

Barrientos, S. (2014). Informe Técnico Terremoto de Iquique, Mw=8.2. Report Centro Sismológico Nacional Universidad de Chile, April 2014.

Brodsky, E. E., and T. Lay (2014). Recognizing Foreshocks from the 1 April 2014 Chile Earthquake. *Science* 344 (6185), 700-702.

Contreras-Reyes, E, J. Jara, I. Grevemeyer, S. Ruiz, and D. Carrizo (2012). Abrupt change in the dip of the subducting plate beneath north Chile. Nature Geoscience, 5, 342-345

Hayes, G. (2014). Updated Finite Fault Results for the Apr 01, 2014 Mw 8.2 99 km NW of Iquique, Chile Earthquake (Version 2). National Earthquake Information Center (NEIC) of United States Geological Survey. http://comcat.cr.usgs.gov/earthquakes/eventpage/usc000nzvd#scientific_finite-fault. Last accessed on 5/25/2014

Podesta, L. F. (2014). Microzonificación Sísmica de las Ciudades de Iquique y Alto Hospicio, Región de Tarapacá. Undergraduate thesis. Escuela de Ingeniería en Obras Civiles, Universidad Diego Portales, January 2014.

2. Performance of Ports

2.1. Port of Iquique

A Google Earth image of the port of Iquique is provided in Fig. 2.1. Performance varied substantially across the port depending on construction procedures, date of construction, and the subsurface soil conditions.

Fig. 2.1. Google Earth image of the entire port of Iquique.

The port consists of the Molo pier which is 530 meters long and the Espigon pier which is 680 meters long as shown in Fig. 2.2. The contrasting performance of the Molo and Espigon piers provides a useful comparison of the effects of soil properties and pier construction during earthquakes. Both piers were originally constructed between 1928 and 1932. A typical cross-section through the Molo pier is provided in Fig. 2.3. The original design for both piers called for large concrete block quay walls to be located on top of mounds of gravel and boulders placed around the perimeter of the pier. The backfill materials were likely dumped into the ocean inside

the quay walls and received little compactive effort. When the Espigon pier was leased to a private operator in 2002, the conditions of the lease required the operator to perform a seismic upgrade to the pier. As part of this upgrade the blocks around the pier were tied together with inclined steel tie-rods. As Fig. 2.3 shows, soil conditions at both piers are different. Under the Molo pier, a layer of medium dense sand ~5 m deep is underlain by ~10 m of dense silty sand, which in turn is underlain by a layer of cemented sand (sandstone). On the other hand, under the Espigon pier, the mounds of gravel and boulders were directly founded on rock.

After the earthquake, the Espigon pier was relatively undamaged and there was no apparent evidence of significant lateral spreading or distress to the pier. As a result of the seismic upgrade, the Espigon pier continued in operation without interruption following the earthquake. In contrast, significant settlement and lateral spreading was observed in the Molo pier. Relative to the perimeter block wall, the interior backfill soil settled between 0.8 and 1.1 meters as shown in photographs in Fig. 2.4. As shown in Fig. 2.2, lateral spreading developed transverse to the direction of the pier over most of the pier with most of the movement towards the east side of the pier. A photograph of the transverse spreading looking towards the north end of the Molo pier is provided in Fig. 2.5 and sand which has vented through cracks in the brick surface after liquefaction is shown in Fig. 2.6. The transverse lateral spread displacement was typically between 0.45 and 0.6 m. The magnitude of displacement increased towards the free-face. In addition, lateral spreading developed in the longitudinal direction along the pier at the far northern end (see Fig. 2.2) creating gaps in the block wall (see Fig. 2.7). The lateral spreading in two orthogonal directions creates a complicated cracking pattern at the end of the pier as shown in Fig. 2.8. Horizontal displacements in the transverse direction were between 1.0 and 1.5 m. The displacement created offset in the block perimeter wall. Observations showed that the lateral spread displacements continued to increase weeks after the earthquake.

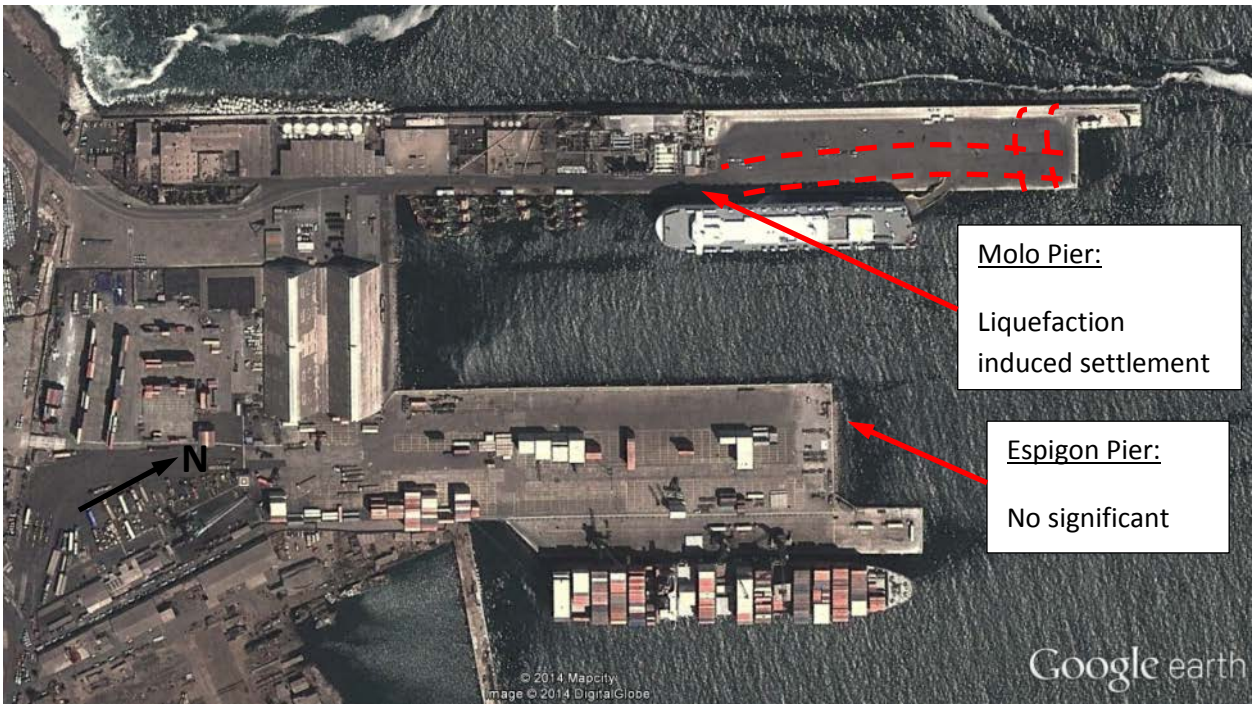

Fig. 2.2 Google earth image focusing on the Molo and Espigon Piers. Liquefaction induced settlement and lateral spread was pervasive on the Molo pier but was not observed on the Espigon pier.

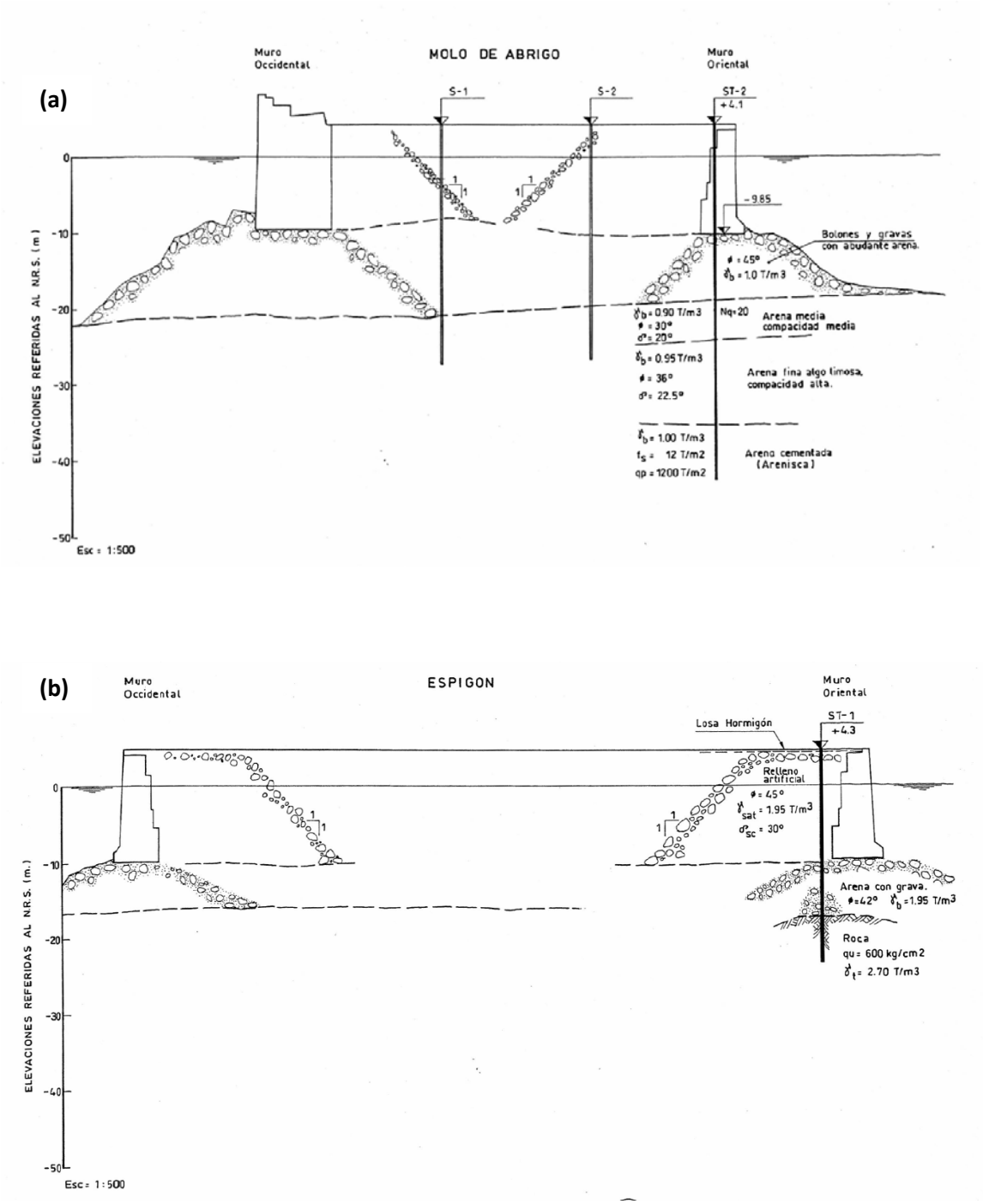

Fig. 2.3 Typical cross-section through (a) the Molo pier and (b) Espigon pier. Large concrete blocks are place on top of piles of gravel and boulders around the perimeter of the pier and backfilled with gravel and sand within the interior of the pier.

-20.202651º -70.157405º

Fig. 2.4 Photos showing typical settlement of backfill soils relative to the perimeter concrete block quay wall. Settlement was typically between 0.8 m and 1.1 m. (-20.202125 º, -70.157684º)

(-20.201491º, -70.157542º)

(-20.202206º, -70.158060º)

Fig. 2.5. Views of lateral spreading cracks running longitudinally along the length of the pier due to transverse displacement towards the east (right).

Fig. 2.6 Photograph showing liquefaction ejecta (sand) which vented upward through brick pavement after formation of cracks from lateral spreading. (-20.202451º, -70.158441º)

Fig. 2.7 Longitudinal offset in the concrete block quay wall along the perimeter of the Molo pier. (-20.200806º, -70.157416º)

Fig. 2.8 Lateral displacement in the longitudinal and transverse directions near the end of the Molo pier. Horizontal displacement in the transverse and longitudinal direction was about 0.6 m and 0.45 m, respectively. The displacement created offsets in the block perimeter wall. (-20.200916º, -70.157139º)

In June 2014, members of the GEER reconnaissance team returned to the Molo pier to coordinate cone penetration (CPT) testing along two lines across the pier as shown in Fig. 2.9. Five CPT soundings were performed to depths of 8 to 23 m using a 30 ton track mounted drill, rig provided courtesy of ConeTec, Inc. Fortunately, this rig, which is normally based in Peru, was performing work at a mine in Northern Chile and the CPT services were donated as the rig was returning back to Peru. Profiles of cone tip resistance, qc for the five soundings along the two lines are provided in Figs.2.10 and 2.11. All the CPT soundings were originally intended to penetrate 20 m, but dense layers prevented this from occurring in four of the five cases. The CPT logs and the original plans suggest that these dense layers were gravelly sands to sandy gravels. However, there were also relatively loose liquefiable sand layers in most CPT profiles.

Fig. 2.9 Locations of CPT soundings and survey lines transverse to the length of the Molo pier.

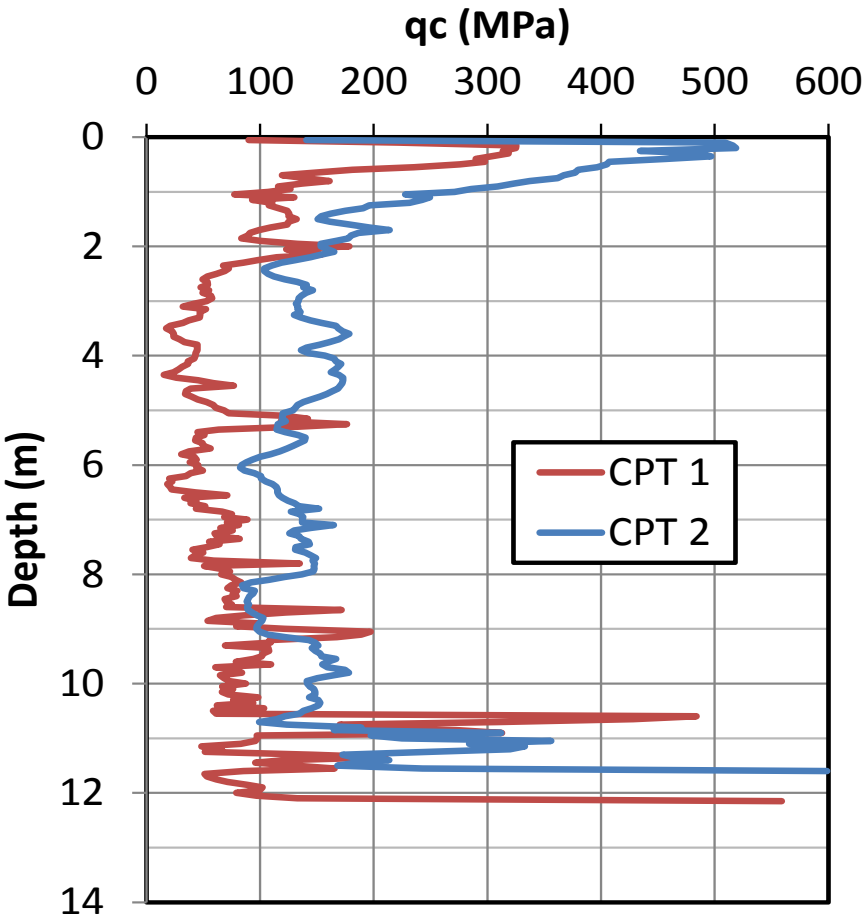

Fig. 2.10 Profiles of cone tip resistance, qc , for CPT1 and CPT2 along a cross-section through the Molo pier as shown in Fig. 2.9.

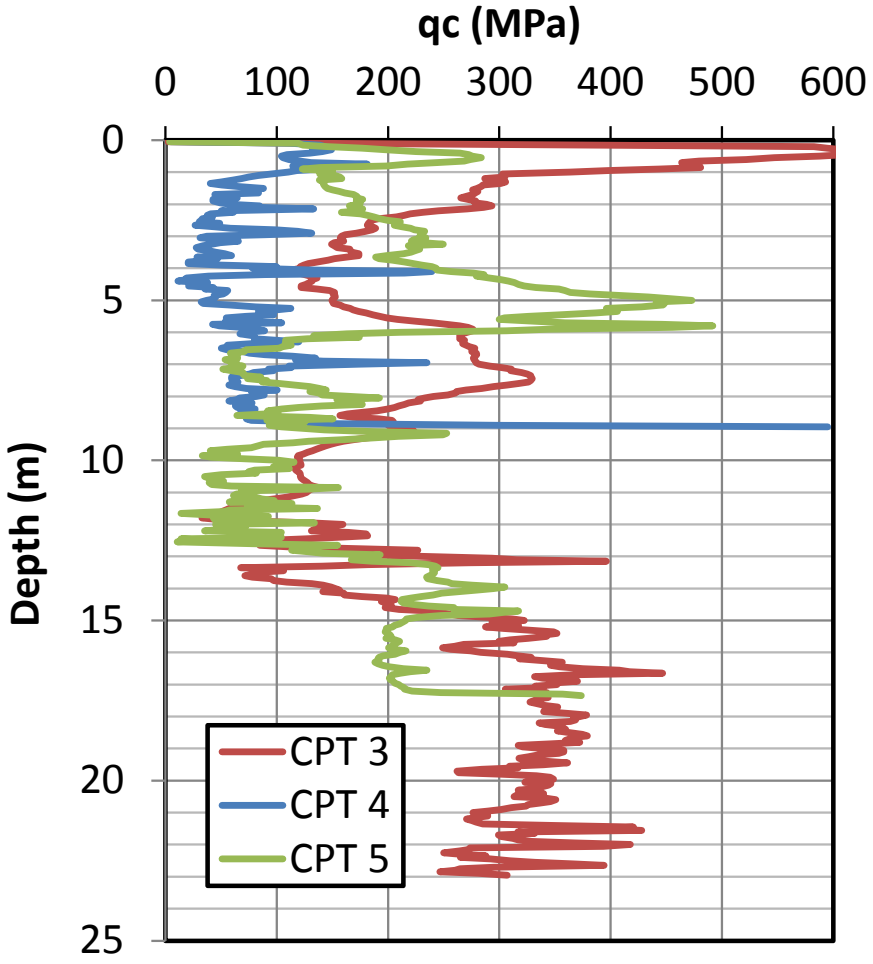

Fig. 2.11 Profiles of cone tip resistance, qc , for CPT3, CPT4 and CPT4 along a cross-section through the Molo Pier as shown in Fig. 2.9.

During the June 2014 visit, the transverse lateral spread displacements were also measured by summing crack widths along three cross-sections along the length of the pier as shown in Fig 2.9. The first line was near CPTs 1 and 2, the second line was near CPTs 3, 4, and 5, and the third section was along the northern edge of the pier. The cumulative displacement versus distance curves are plotted for the three sections in Fig. 2.12 and the profiles are relatively consistent. The maximum displacements at this point had increased to 1.5m and 2.1m on two of the cross-sections, which represents an increase of about 0.5 m relative to that observed a couple weeks after the earthquake. This additional displacement appears to be associated with movement between 6 to 14 m from the west edge of the pier. The cumulative displacement curves indicate that the middle section from about 18 to 36 m from the west side moved as a block, while displacements increased significantly approaching the east edge of the pier.

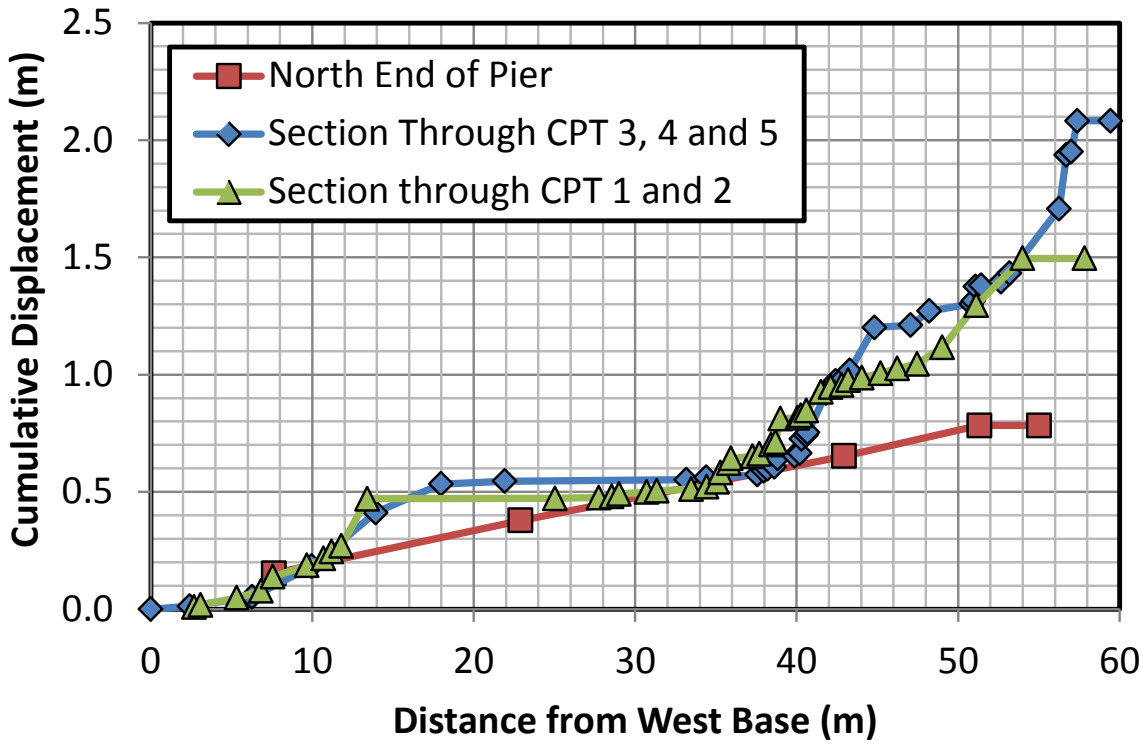

Fig. 2.12 Cumulative lateral spread displacement vs. distance curves through three transverse sections through the Molo pier.

Also in June 2014, members of the GEER reconnaissance team returned to the Molo pier with an unmanned aerial vehicle (UAV) to demonstrate the potential uses of these platforms in post-earthquake geotechnical reconnaissance. The UAV flown at the Molo pier was a DJI® Phantom II Vision+ quad-rotor with a GoPro® Hero 3+ camera. The GoPro® camera had a customized 5.4mm flat lens, and collected 1080p High Definition video of the pier.

Images from the UAV flight were subsequently processed using Agisoft® PhotoScan software, and three-dimensional reconstructions of the pier were developed in the form of a dense point cloud. Still frames (2.76 Mpixel resolution) were manually extracted from the GoPro HD video and were processed with the PhotoScan software. In total, 466 still frames were processed in the model. Pre-processing of the images was performed beforehand to remove "noise" from individual photographs that might negatively impact the computer vision processing. The resolution of the resulting model is approximately 5.5 cm. Research is currently being conducted to geo-reference the point cloud model using surveyed measurements of the pier. Displacements measured at the pier are also currently being evaluated and compared against displacement measurements taken from the dense point cloud model. Figs. 2.13 through 2.16 present screenshots of the dense point cloud model of the Molo pier. Once geo-referenced, the dense point cloud model will be given to GEER for researchers to access.

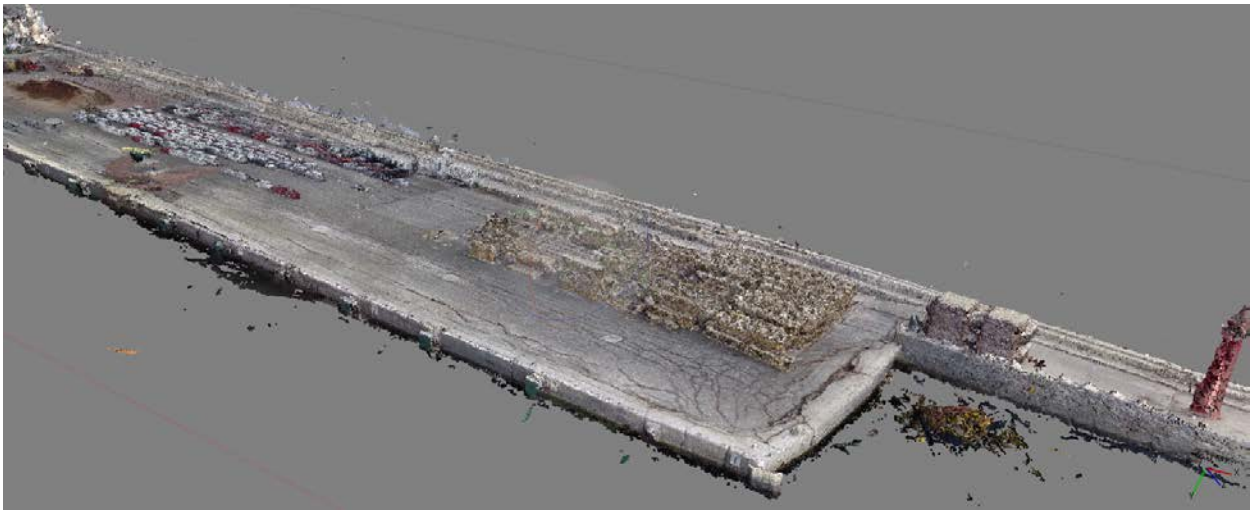

Fig. 2.13 Screenshot of the Molo pier dense point cloud developed from UAV-based photographs taken in June 2014

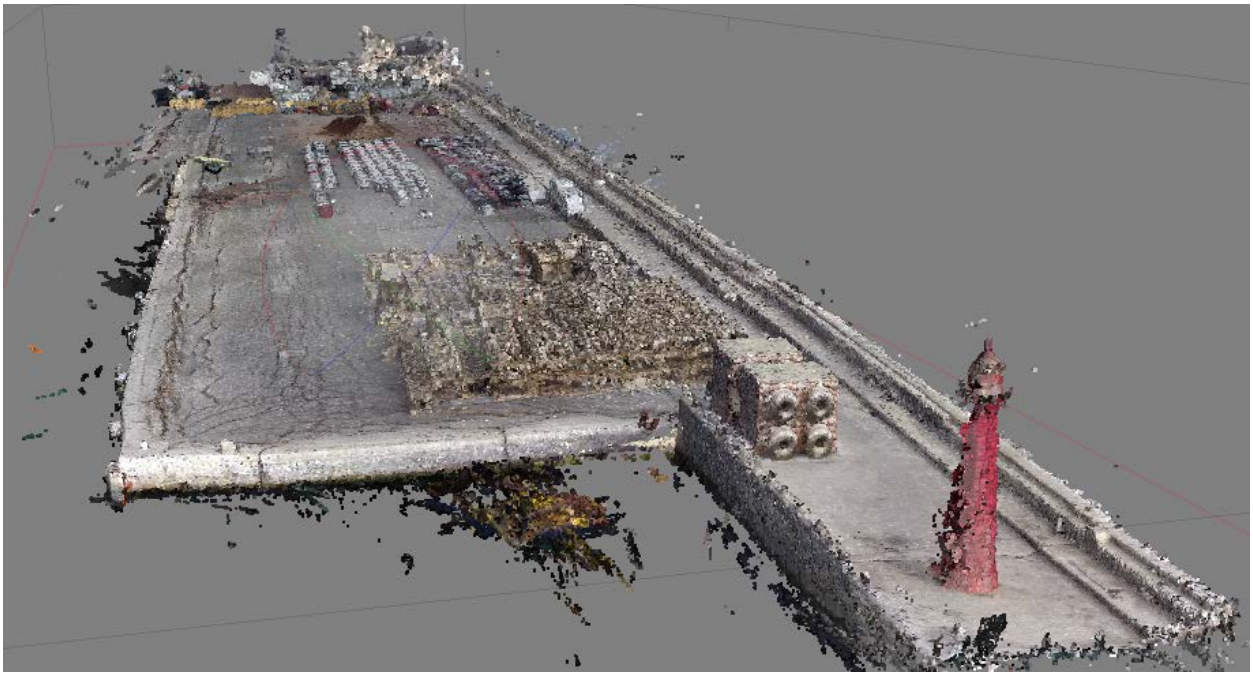

Fig. 2.14 Screenshot of the edge of the Molo pier dense point cloud

Fig. 2.15 Screenshot of corner cracking and deformation from the dense point cloud

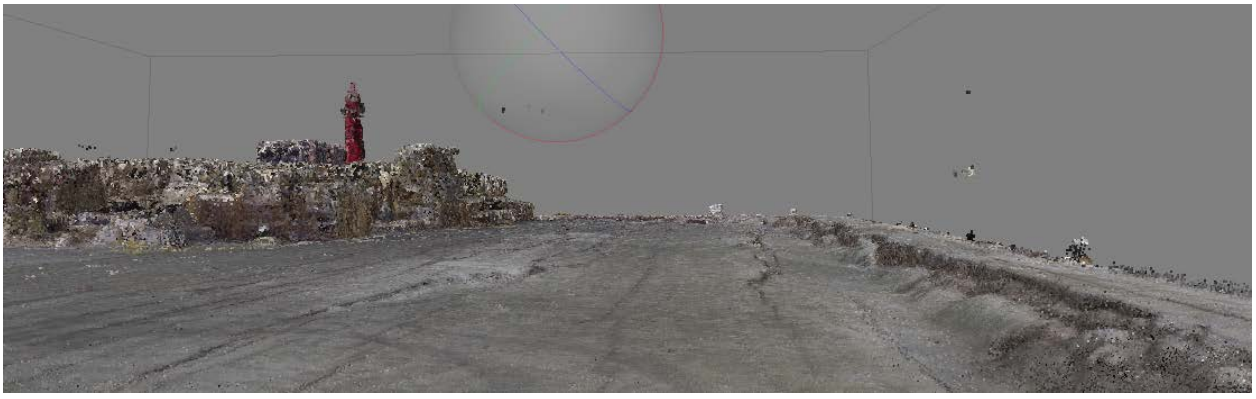

Fig. 2.16 Screenshot of cracking and slumping at the pier surface from the dense point cloud

2.2. Port of Arica

A Google Earth image of the man-made port in Arica is shown in Fig. 2.17. No first-hand visits were made to this port during the post-earthquake investigation; however, reports from the Chilean Army Corps of Engineers indicated that damage to the port was relatively minimal and that operation of the facility was not impaired, which is consistent with the information provided by the Ports Department of the Ministry of Public Works (MOP). Fig. 2.18 shows some photos of the port that were taken nine days after the earthquake.

Fig. 2.17 Google earth image of the port at Arica.

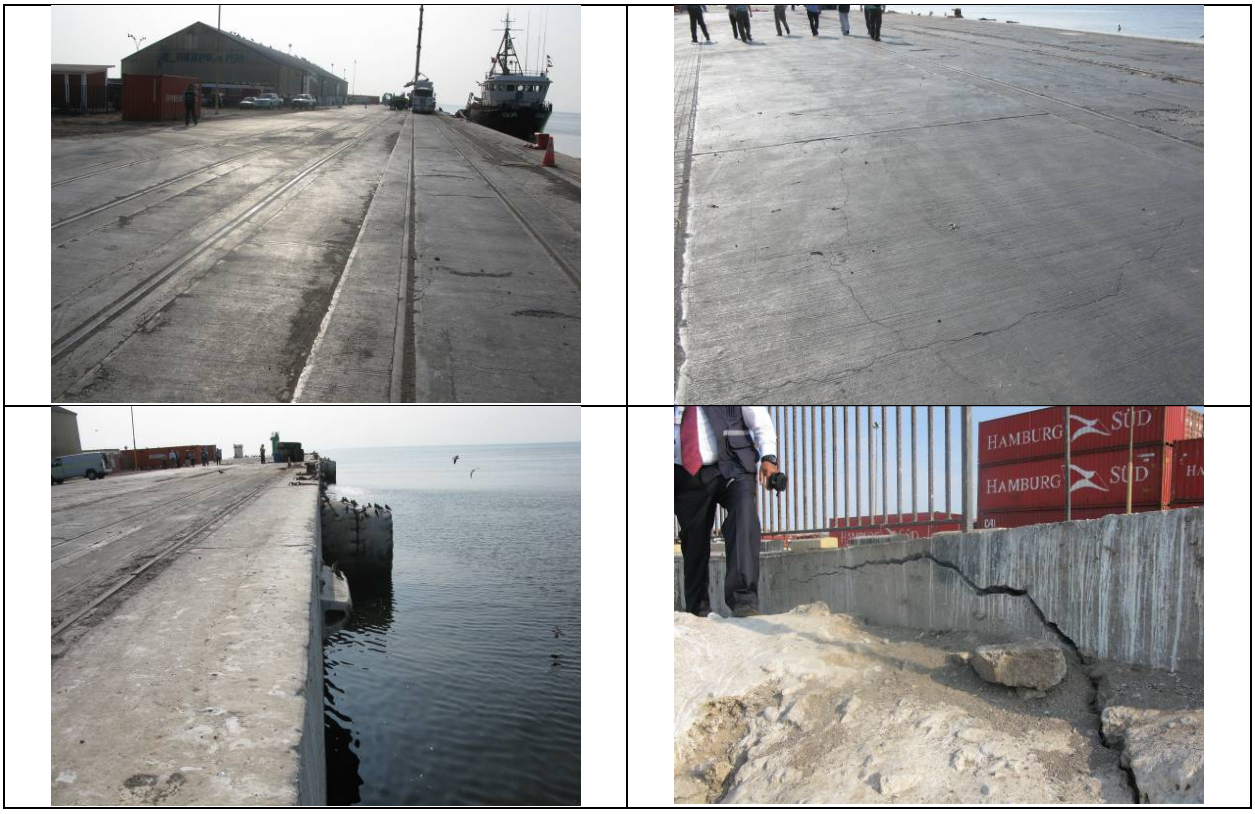

Fig. 2.18 Images of the port at Arica after the earthquake. (Locations unavailable)

3. Performance of Bridges

Three significant bridges along Route 5 between Iquique and Arica were subjected to strong ground shaking. The locations of the Camarones, Tana, and Tiliviche bridges are shown on a Google Maps image in Fig. 3.1. These bridges pass over river channels flowing westward through the desert and into the Pacific Ocean.

Fig. 3.1 Google Earth image showing location of three bridges on Route 5 between Iquique and Arica, Chile

3.1 Tiliviche Bridge

The Tiliviche bridge is a curved steel girder bridge consisting of three spans, each about 22 m in length. The curve is laid out along a radius of about 130 m and transects an arc of about 20º as shown in Fig. 3.2.

Fig. 3.3 shows a photo of the bridge looking from the western side and it may be seen that the bridge piers consist of solid concrete walls. An examination of the lines across the bridge deck indicates that there was no appreciable offset at any of the bridge joints located at the abutments and pier supports. In addition, there was no evidence of vertical offsets.

Fig. 3.2 Google Earth image of the curved Tiliviche Bridge composed of three simply supported segments (-19.551966º, -69.940921º).

Fig. 3.3. Photo of the Tiliviche bridge elevation (-19.551966º, -69.940921º).

Very little water was flowing in the stream channel under the bridge at the time of the earthquake and there were no sand boils indicating liquefaction. The only distress observed in the vicinity of the bridge was a series of cracks, about 20 to 30 mm wide, which ran parallel to a stream channel for a distance of about 10 m as shown in Fig. 3.4.

Fig. 3.4 Photograph showing cracks paralleling the stream channel below the Tiliviche bridge (-19.551966º, -69.940921º).

3.2 Tana Bridge

The Tana bridge is a curved steel girder bridge consisting of five spans of about 16 to 18 m in length. The curve is laid out along a radius of about 90 m and transects an arc of about 50º as shown in Fig. 3.5. Fig. 3.6 shows a photo of the bridge looking from the northwestern side and it may be seen that the bridge piers consist of solid concrete walls. Despite the curvature of the bridge, an examination of the lines across the bridge deck indicated that there was no appreciable offset at any of the bridge joints located at the abutments and pier supports. In addition, there was no evidence of vertical offsets. Finally, there were no significant cracks in the support piers or abutments.

Gabion walls were used to stabilize the steep slopes running west from the north abutment as shown in Fig. 3.5. The photograph in Fig. 3.7 shows cracking in the ground surface at the top of the slope adjacent to the gabion wall along the north slope. Crack widths suggest wall movements on the order of 30 to 60 mm. The photographs in Fig. 3.8 show (a) the terraced gabion wall immediately to the west of the north bridge abutment and (b) a cross-section through the gabion and soil mass behind the gabions. Tension cracking is visible at the interface between the bridge abutment and soil mass in the photo in Fig. 3.8(b). Several cracks were also observed running perpendicular to the abutment wall in the gabion supported slope immediately adjacent to the north abutment.

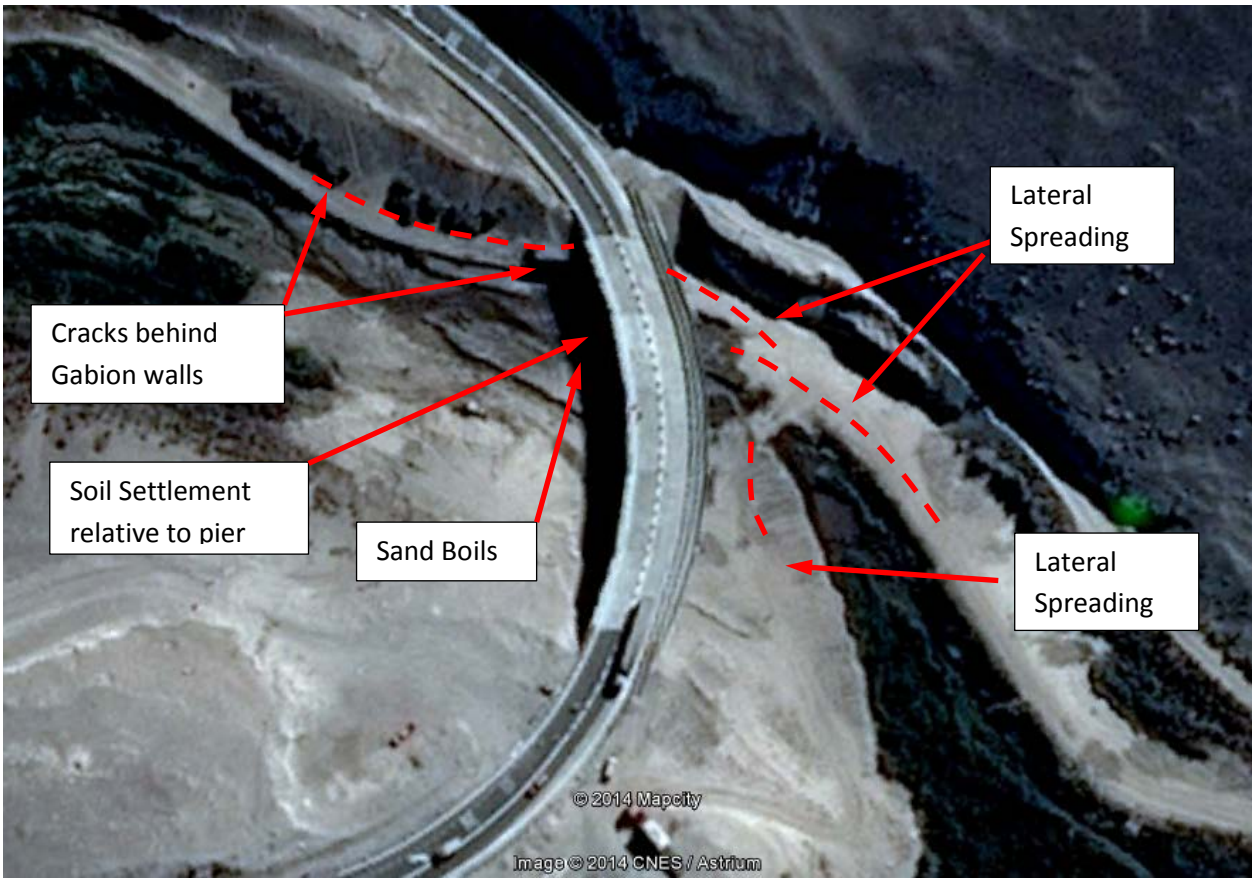

Fig. 3.5 Google Earth image showing plan view of Tana Bridge (-19.454491º, -69.946831º).

Fig. 3.6 View of the bridge from the southwest showing gabion walls against the abutment in the foreground. (-19.454491º, -69.946831º).

Fig. 3.7 View of cracking behind gabion wall running parallel to the north abutment and river slope. Largest crack widths are approximately 20 to 40 mm. (19.454135°, -69.946804°)

Fig. 3.8 (a) Gabion wall adjacent to the north bridge abutment and (b) tension crack adjacent to abutment behind gabion wall. (19.454265°, -69.946496°)

The original plans for the bridge indicate that the soil profile consists primarily of poorly graded gravel (GP) to a depth of about 25 m with a surface layer of silty sand (SM) about 1.5-m thick. The plans indicate that each pier is supported by six 150 cm-diameter piles (drilled shafts) which extend 15 m below the pile cap into the gravel layer. The abutments are supported by eight 150 cm-diameter piles which extended 12 m below the base of the pile cap into the gravel layer.

Although there was no evidence of distress to the bridge, a number of liquefaction features were evident in the alluvial soil deposits beneath the bridge. A photograph showing several sand boils located just downstream of the first bridge pier south of the north abutment is provided in Fig. 3.9. While the ejecta is primarily sand, it is unclear at this point whether or not the gravel in the profile also liquefied. The liquefaction may have been limited to sand zones relatively close to the stream, although there is insufficient information to make this determination at the present time. Liquefaction induced settlement produced an offset of approximately 15 cm adjacent to the bridge pier as shown in Fig. 3.10.

Liquefaction in the soil profile adjacent to the Tana river also led to lateral spreading. The lateral spread extended approximately 80 m along the north side of the river running southeast from the bridge abutment as shown in Fig. 3.5. –A photograph of the lateral spread from the north abutment looking to the southeast is provided in Fig. 3.11. Although the lateral spread impinged upon the north bridge pier, the ground movement was insufficient to cause distress to the pier. In fact, it appears likely that the presence of the pier was sufficient to limit the ground movement resulting from liquefaction relative to locations away from the bridge.

The photograph in Fig. 3.12 shows a closer view of the slumping near the head of the spread. The slope of the ground at this location was about 10º and the vertical offset relative to the stream was about 1.5 m. The lateral spread extended approximately 10 m behind the stream bank and lateral displacements were estimated to be between 0.3 and 0.6 m.

A series of 212 photographs taken with a Sony® NEX-5R camera were used with the structure from motion (SfM) computer vision software VisualSFM to develop a three-dimensional (3D) computer reconstruction of a portion of the lateral spread at the Tana bridge. The resulting computer vision model includes over 1,300,000 mesh elements. A screenshot of the computer vision model is presented in Fig. 3.13. The model was developed to investigate the potential usefulness of computer vision models in characterizing future liquefaction hazard sites, and shows significant promise for rapidly capturing surface topographic details. Such models could be a useful addition to tools like terrestrial laser scanners for performing site reconnaissance and detailed surface site characterization.

Members of the reconnaissance team return to the Tana bridge in June 2014 with a custom-built hex-rotor unmanned aerial vehicle capable of carrying a large Nikon® D7100 DSLR camera. The camera captured a 24Mpixel image every three seconds. Two flights, each lasting approximately 15 minutes, were used to gather close to 600 photographs from the bridge and surrounding liquefaction damage. The photographs were then filtered to remove any images with excessive blur. Agisoft® PhotoScan was used to process the remaining images and to develop a high density 3D point cloud of the site. Screenshots of the resulting model is presented in Figs. 3.14 and 3.15. The resolution of this model is approximately 1 cm.

Fig. 3.9 Photograph of sand boils adjacent to small stream flowing beneath the Tana bridge. (19.454245°, -69.946399°)

Fig. 3.10 Photograph showing settlement of soil adjacent to bridge pier as a result of liquefaction. (19.454245°, -69.946399°)

Fig. 3.11. Photograph showing lateral spreading running parallel to stream channel flowing under the Tana bridge. (19.454013°, -69.946349°)

Fig. 3.12 Photograph showing closer view of lateral spreading running parallel to stream channel flowing under the Tana bridge. (19.454418°, -69.945864°)

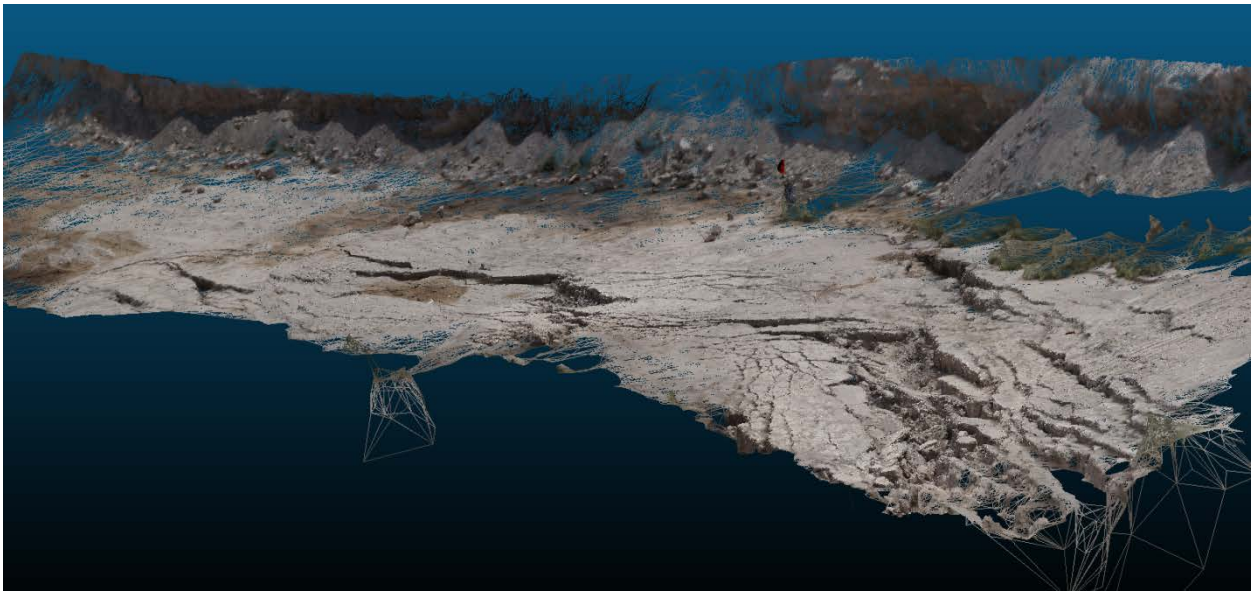

Fig. 3.13 Screenshot of a SfM computer vision 3D reconstruction of a portion of the Tana bridge lateral spread. (19.454389°, -69.945953°)

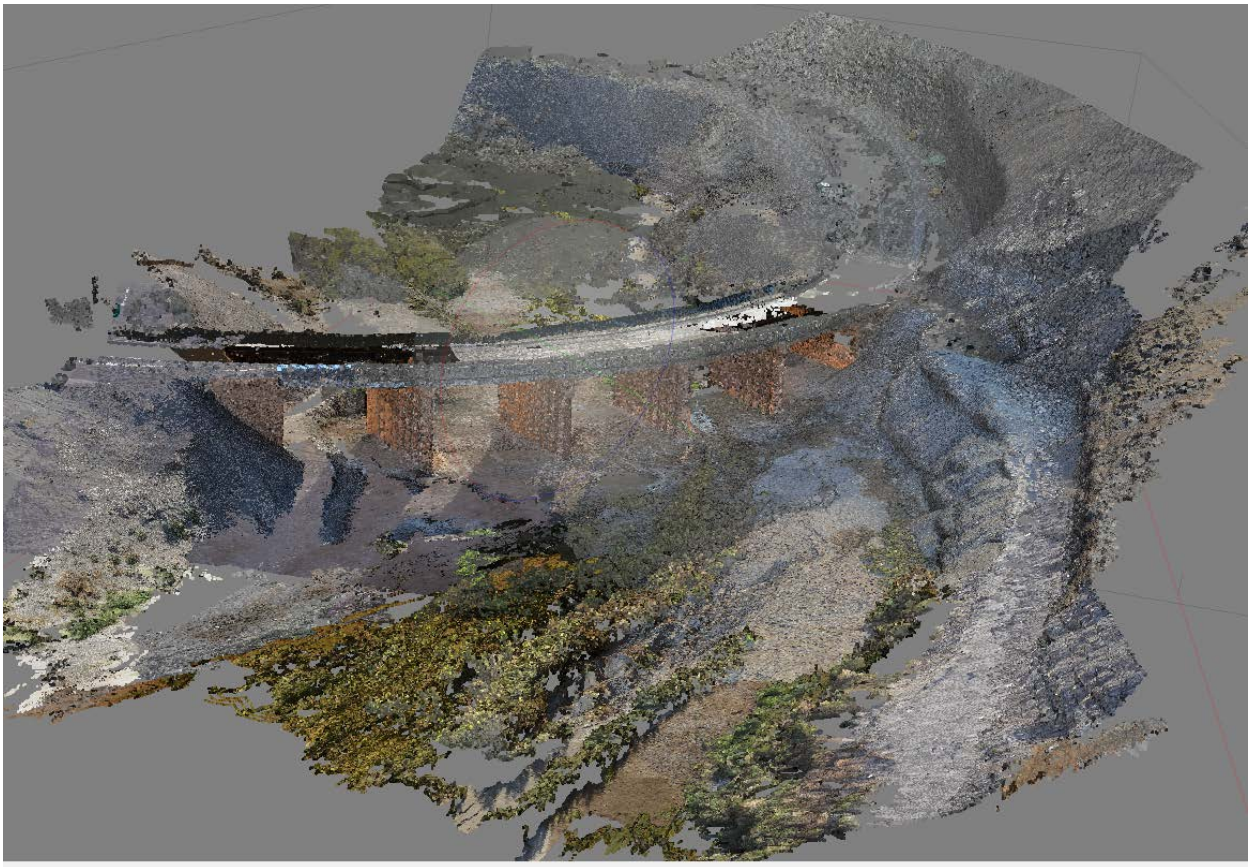

Fig. 3.14 Screenshot of a SfM computer vision 3D reconstruction of the Tana bridge, developed from UAV-based photographs

Fig. 3.15 Screenshot of a SfM computer vision 3D reconstruction of the lateral spread adjacent to the Tana bridge, developed from UAV-based photographs

3.3 Camarones Bridge

The Camarones bridge is a steel girder bridge consisting of eight spans each about 30 m in length. Fig. 3.16 shows a photo of the bridge. At the time of the reconnaissance, the bridge was closed to traffic due to a lateral offset of approximately 10-15 cm between two of the spans as shown in Fig. 3.17. Unfortunately, the bridge closure prevented closer inspection of the superstructure at the time of the reconnaissance.

Relatively little evidence of soil liquefaction was observed in the alluvial sediments beneath the bridge, and little structural or foundation damage to the bridge was observed. Fig. 3.18 presents an overview of the reconnaissance observations at the bridge. A sand boil approximately 60 cm in diameter was observed within about 10 m of the third bent from the northwest abutment (Fig. 3.19). Small settlements of approximately 5-10 cm were evident in the fill surrounding the northwest abutment.

Fig. 3.16 Photograph of the Camarones Bridge. (-19.157123°, -70.187611°)

Fig. 3.17 Photograph of lateral offset observed at the Camarones Bridge. (-19.007839°,-70.002497°)

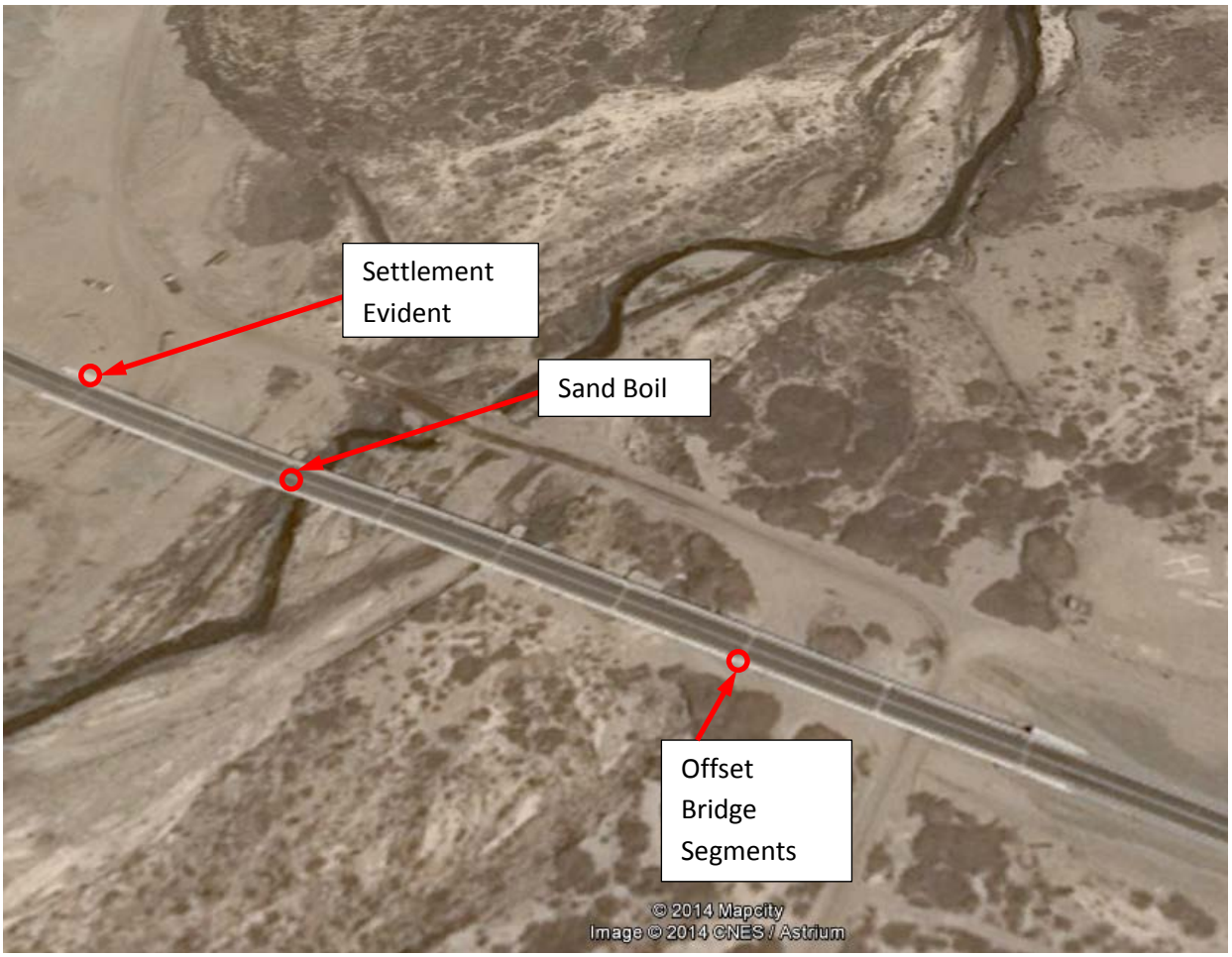

Fig. 3.18 Google maps image of the Camarones Bridge composed of eight simply supported segments (-19.157493º, -70.186478º).

Fig. 3.19 Sand boil observed at the Camarones Bridge (-19.157366º, -70.186806º).

4. Performance of Retaining Structures

Despite the large intensity of the earthquake, the overall performance of retaining structures in Iquique was acceptable and in good agreement with the measured ground accelerations. Retaining walls with significant damage were observed at three locations: Cerro Dragon, the Municipal Stadium, and the Fishing piers at Caleta Riquelme. These structures consisted of masonry or concrete walls without adequate footings and retaining a dry loose backfill. A mechanically stabilized retaining wall in the south end of Cerro Dragón collapsed a result of advanced corrosion in the soil reinforcement. No damage was observed in basement walls or temporary braced excavations.

4.1 Retaining walls of Cerro Dragón

Several retaining walls in *Los Algarrobos* street at Cerro Dragon were damaged due to the insufficient size of the footing, the lack of restraining elements, and the low strength of the backfill. The observed failure mode was overturning, with measured tip displacement varying between $\Delta/H=8\%$ at the north end and $\Delta/H<1\%$ at the south end, as shown schematically in the Google earth photograph of Fig. 4.1. The extent of the damage was significant considering that peak ground acceleration at the site was less than 0.25g.

Fig. 4.1. Google earth photograph of the housing development of Cerro Dragón

These retaining walls are made of reinforced concrete, have a thickness of 20 cm, a height of 240 cm and spans between 3 m and 15 m. The walls are part of a development built on the dunes of

Cerro Dragon, where the terrain is made primarily of loose marine sands, poorly graded particles (C_u=0.50, C_c=0.80) of medium to small size (d_{50}~0.2mm), and a friction angle between 30°-35°. Additionally, these soils have significant amount of calcareous sediments and soluble salts, which increases the risk of bearing capacity failures and large settlements induced by water infiltrations. The backfill was flat and the material was loose dune sand mixed with debris, and no moisture content.

The largest measured overturning was approximately 20 cm (Δ/H=8%), as shown in Fig. 4.2. Based on a photograph taken before the 2014 Iquique earthquake, it is concluded that all the deformation occurred during this event. Large rotations were observed on other walls along *Los Algarrobos* street, however these walls had already overturned, presumably after the 2007 Tocopilla earthquake (M_w=7.7) and 2005 Tarapacá earthquake (M_w=7.8), and had not been retrofitted since (Fig. 4.3). Large rotations on a retaining wall induced backfill displacements and differential settlements on the house shown in Fig. 4.4. Following the earthquake, people blocked the streets and abandoned their houses. A number of non-engineered retaining walls tipped over as shown in Fig. 4.5. However, it is interesting that most of the walls with almost no reinforcement did not collapse!

Fig. 4.2. Retaining wall in Los Algarrobos Street 20°15'43"S - 70°07'24"W.
Left: wall before the earthquake, source Google Street View.
Right: wall displaced after the earthquake (Δ/H=8%)

Fig. 4.3. Retaining walls damaged in previous earthquakes. The gaps were filled with mortar, piping, and vegetation or in some cases left empty. (20°15’43”S - 70°07’24”W)

Fig. 4.4. Left: Signs reading "closed due to failure" and "do not trespass, bad wall" in Los Algarrobos Street. Right: retaining wall displacement (Δ/H=4%) induced large backfill displacements and structural damage to the houses. (20°15'43"S - 70°07'24"W)

Fig. 4.5 Failure of unreinforced non-engineered retaining walls. (-20.246503°, -70.129301°)

4.2 Retaining walls at Municipal Stadium

A 20 m section of a masonry wall (h=150 cm) located at the Municipal stadium "Tierra de Campeones" was severely damaged as a result of the ground motion (Fig. 4.6). The wall was sitting atop of a 2:1 slope 3 m high, and had a flat backfill made of dry loose sand. The failure mode was an outward tilting and displacement caused by the absence of a footing or other restraining elements. No signs of a global failure were observed.

Fig. 4.6. Left: Aerial view of retaining walls at the Municipal Stadium (-20.243611°, - 70.132222°). Right: overturning failure of masonry walls at the Municipal Stadium

4.3 Mechanically Stabilized Earth Structures (MSE)

In general, the performance of mechanically stabilized earth structures was acceptable, including overpasses and bridge abutments. No major damages were observed, with the exception of the retaining walls that collapsed near the south end of Cerro Dragón, at the intersection of *Los Algarrobos* and *Cuatro Sur* streets. These MSE walls formed a three level terrace to hold a parking garage and a public road, as seen schematically in Fig. 4.7 and in the photograph of Fig. 4.8 taken before the earthquake.

As a result of the advanced state of corrosion in the soil reinforcement, added to the seismic loads on the backfill, approximately 60 m of wall in the 3rd level collapsed as shown in Fig. 4.8. Localized failure of the walls in the first level was also observed, as shown in Fig. 4.9. The failure mode was the rupture of the steel reinforcement and internal stability of the reinforced soil mass. The backfill material was the marine sands of Cerro Dragón, which have an enormous corrosion potential due to the presence of soluble salts (chlorides and sulfates), and the free exchange of moisture between the soil and the air. The steel reinforcement, shown in Fig. 4.10, was made of ϕ10 mm bars hot-dip galvanized. In non-aggressive media, this reinforcement

would have performed well, but the highly corrosive soils present at the site, led to a rapid reduction of the zinc coating and reduction of the rebar cross section, affecting the load bearing capacity of the wall.

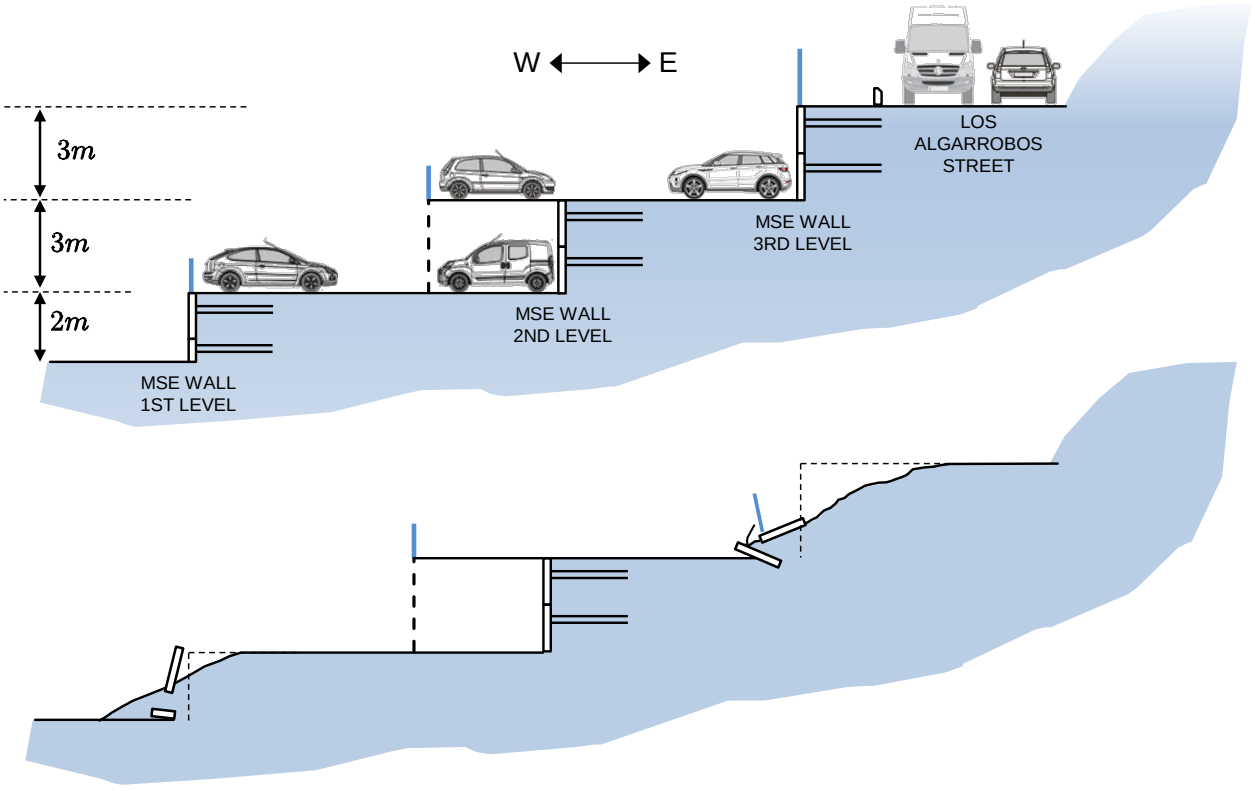

Fig. 4.7 Top: schematic elevation of MSE retaining walls of the parking garage of "Condominio Horizontes". Bottom: schematic view of the failure mode

Fig. 4.8 Photograph of retaining walls before the earthquake. Source: Google Street View (20.273889°, - 70.123889°)

Fig. 4.9. Failure of retaining walls in the upper level and backfill displacements (20.273889°, - 70.123889°) (photograph courtesy of Ramon Verdugo)

Fig. 4.10. Localized failure in the 1st level and backfill flow (20.273889°, - 70.123889°) (photograph courtesy of Ramon Verdugo)

Fig. 4.11. Advanced corrosion of the galvanized steel bars (20.273889°, - 70.123889°) (photograph courtesy of Ramon Verdugo)

4.4 Basement walls and temporary excavations

Basement walls are rare in Iquique since the bedrock is typically found at shallow depths. Of those basements visited, including high rise reinforced concrete structures, no signs of damage

were observed. Likewise, the temporary excavations of route A-16 in Alto Hospicio remained stable and no reports of damage were issued (see Fig. 4.12).

Fig. 4.12. Undamaged basement walls of buildings ‘Punta Cavancha’ (Left) and ‘Hotel Terrado’ (Right)

5. Ground Response

5.1. Available information prior to earthquake and records

Prior to the earthquake, a seismic microzoning had been proposed for Iquique and Alto Hospicio cities based on geophysical data, boreholes and geological background (Becerra et al., 2014). This study suggests zones that are most prone to site effects, namely: III-B, IV-B and V-B in Fig. 5.1. Additionally, the recorded PGAs (www.sismologia.cl) are shown in the same figure, and they are in good agreement with the proposed microzoning. The minimum PGA (0,27g) is located in a zone characterized as bedrock, whereas the maximum (0,6g) was registered where marine deposits of moderate thickness was found, which indicate the effects of relatively soft soil layers on the ground amplification. In the case of Alto Hospicio city, the recorded acceleration has a PGA of 0.44g, in agreement with the stiff soils detected in the study conducted by Becerra et al. (2014). The waveforms of the recorded motions are displayed in Fig. 5.2.

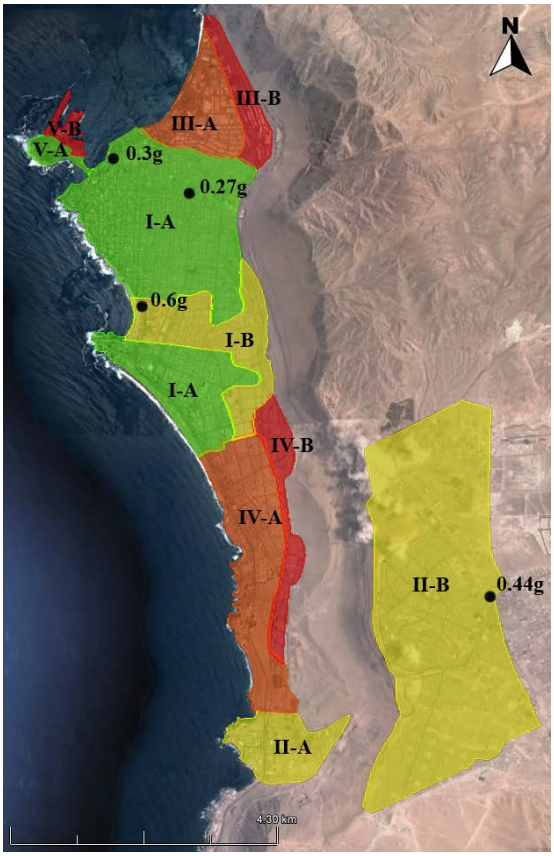

Color	Zone	Avg. V_s^{30} [m/s]	Freq. range [Hz]	Description
Iquique				
	I-A	872 ± 183	$[0.22 - 1.77]$	Andesite outcrop.
	I-B	768 ± 166	$[3.46 - 10.22]$	Marine and eolian deposits, bedrock located at 5 to 15 meters deep.
	II-A	577 ± 86	$[1.7 - 5.15]$	Colluvial deposits, bedrock located at 5 to 15 meters deep.
	II-B	709 ± 108	$[1.13 - 1.45]$	Gravels from Alto Hospicio, stiff layer of gravels of about 15 meters until bedrock.
	III-A	461 ± 50	$[1.2 - 7.6]$	Marine deposits, bedrock at deep levels.
	III-B	612 ± 35	$[3.25 - 4.1]$	Eolian and marine deposits, bedrock is located about 25 meters deep.
	IV-A	403 ± 38	$[3.03 - 4.68]$	Eolian deposits of over 30 meters deep.
	IV-B	379 ± 48	$[1.83 - 2.86]$	Eolian and alluvial deposits from El Dragon hill, consisting mostly of fine sand, bedrock at deep levels.
	V-A	762 ± 205	$[6.84 - 16.85]$	Andesite outcrop in the port of Iquique.
	V-B	393 ± 78	$[2.46 - 5.74]$	Artificial landfill from the port of Iquique.

Fig. 5.1. Seismic microzoning of Iquique (Becerra et al., 2014)

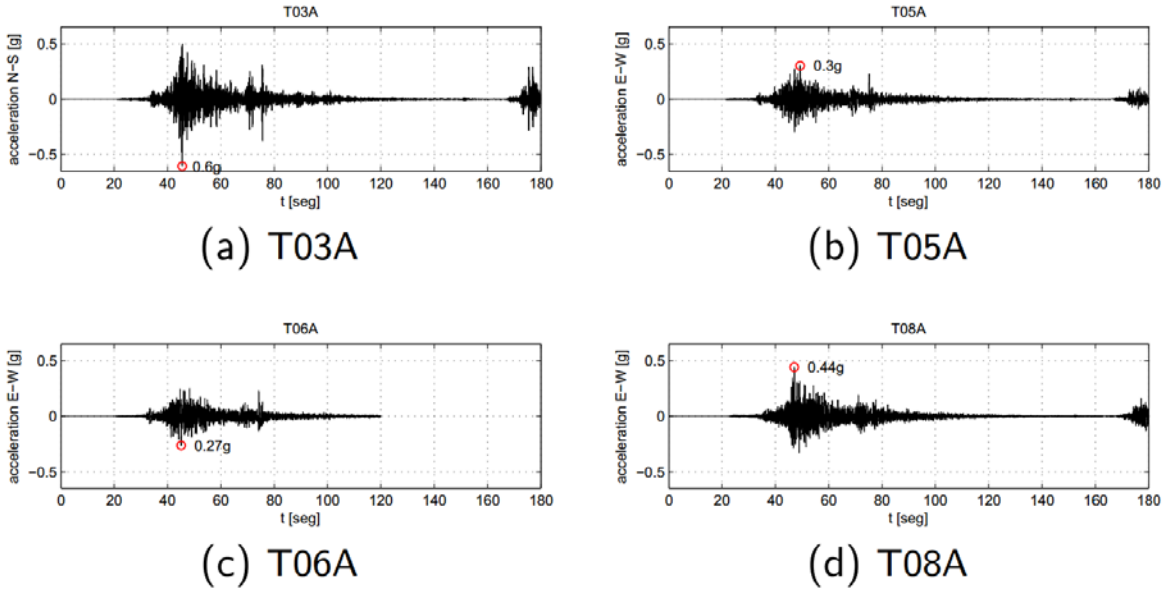

Fig. 5.2. Acceleration records of the 01A-2014 provided by the National Office of Emergency (ONEMI). Stations T05A and T06A are located in zone I-A, T03A is in zone I-B and T08A is placed in Alto Hospicio (zone II-B)

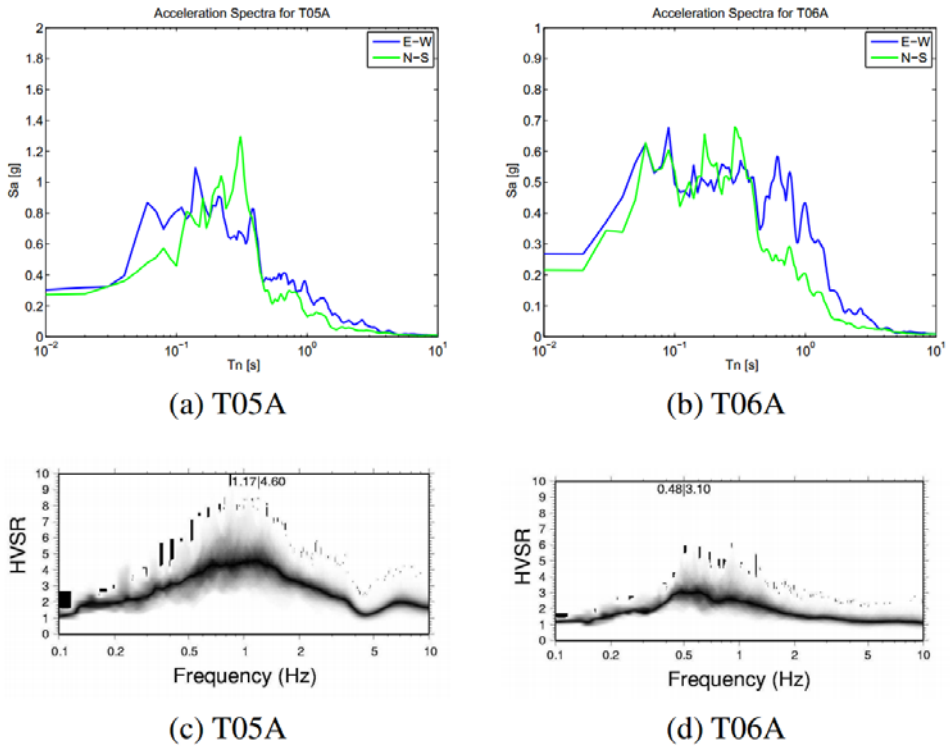

Fig. 5.3. Acceleration Spectra for stations located in outcropping bedrock (zone I-A) and comparison to Nakamura's results

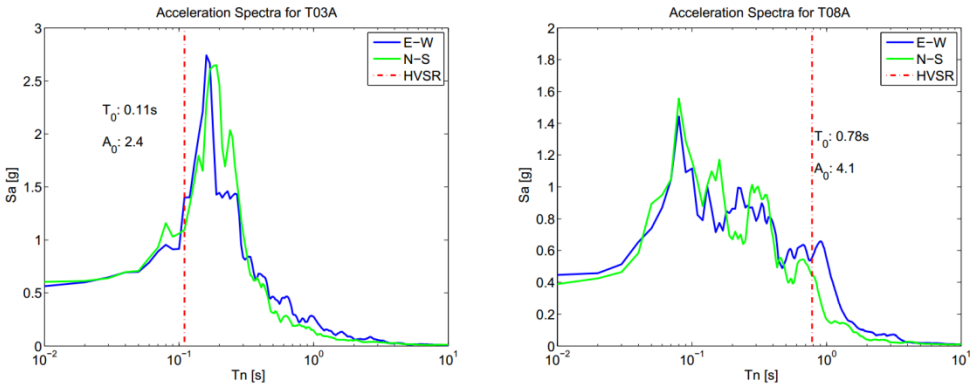

(a) T03A (b) T08A

Fig. 5.4. Acceleration spectra for stations T03A and T08A located on different soils. The red dotted line and text on the Figures represent the Nakamura's result for the closest site.

Furthermore, the acceleration spectra of each record were computed with a damping ratio of 5%. The results of the stations located in bedrock are shown in Fig. 5.3. These spectra are characterized for their wide shape and low amplitude, in agreement with the results of the previously performed Nakamura's test close to the respective seismic station. It can also be noted that for station T05A the peaks are considerably different in the N-S and E-W orientations. The T05A station is located at 1800 meters from the Coastal Range's escarpment. Hence, these variations could be explained through the reflected wavefield at the escarpment (Becerra, 2014). However, further studies are required to validate this hypothesis.

The acceleration spectra for stations located on soil are displayed in Fig. 5.4. Note that for station T03A, the peak period of the spectra is slightly higher than the predominant period obtained from a closely located Nakamura's measurement (of about 100 meters). This could be caused by the non-linearity of the soil behavior. Nonetheless, to confirm this hypothesis, an additional measurement located in the same position as the seismic station is required in order to discard the existence of local differences on the thickness of the sediments.

Station T08A does not compare to Nakamura's predominant period at all (Fig. 4b), possibly because of the high stiffness of the soil in Alto Hospicio city, which would behave almost as outcropping bedrock (hence the lower amplitudes).

Based on this scenario, the damage reconnaissance campaign after the earthquake focused on zones where ground motion amplification was likely to occur. Three cases of interest were identified in which site effects may have had a significant influence in the observed damage. These cases are located in the cities of Iquique and Alto Hospicio and they are displayed in Fig. 5.5. A summary of our observations are described in the following.

Fig. 5.5. Location of cases of study

5.2 ZOFRI

The ZOFRI is an industrial zone composed of mainly three to five levels confined masonry warehouses. Most of this zone is characterized by a moderate to thick layer of marine deposits. Towards the east, the thickness of this layer decreases (to about 20 meters) and mixes with eolian deposits. There is also an important effect of the escarpment located to the east.

The observed damages in the zone are classified by type in Fig. 5.6. Most of it concentrated in the roof parapets, whereas few structural damage and landslides were identified in the area (Fig. 5.7 and Fig. 5.8). The soft soil layer and the topographic effects of the escarpment could have caused higher accelerations in the zone, resulting in larger damage in structural and nonstructural components, such as the roof parapets. Fig. 5.9 shows the predominant frequency of each site obtained through H/v ratios or Nakamura's technique (Nakamura, 1989) after the earthquake. This figure also displays the amplitude of these H/V ratios. It can be noted that higher amplitudes characterize the data towards the east, which suggests a significant impedance contrast between the soil layers and the bedrock. This result would strengthen the hypothesis of ground motion amplification around this area. However, this cannot be confirmed by records because no seismographs were installed in this sector during the earthquake.

The slopes located to the east of the ZOFRI zone have terraces that were built solely under shallow compaction to allow vehicle transit, without any reinforcement or containment systems. Therefore, the landslides shown in Fig. 5.8 were foreseeable. During the reconnaissance campaign, we measured a maximum horizontal slide of 1.3 meters by adding the opening of the cracks across straight lines parallel to the direction of sliding.

Fig. 5.6. Observed damage in the ZOFRI zone

Fig. 5.7 (left) Typical short column structural damage and (right) fallen roof parapets in the ZOFRI zone.

Fig. 5.8. Observed landslides in the ZOFRI area (-20.200965º, -70.128995º)

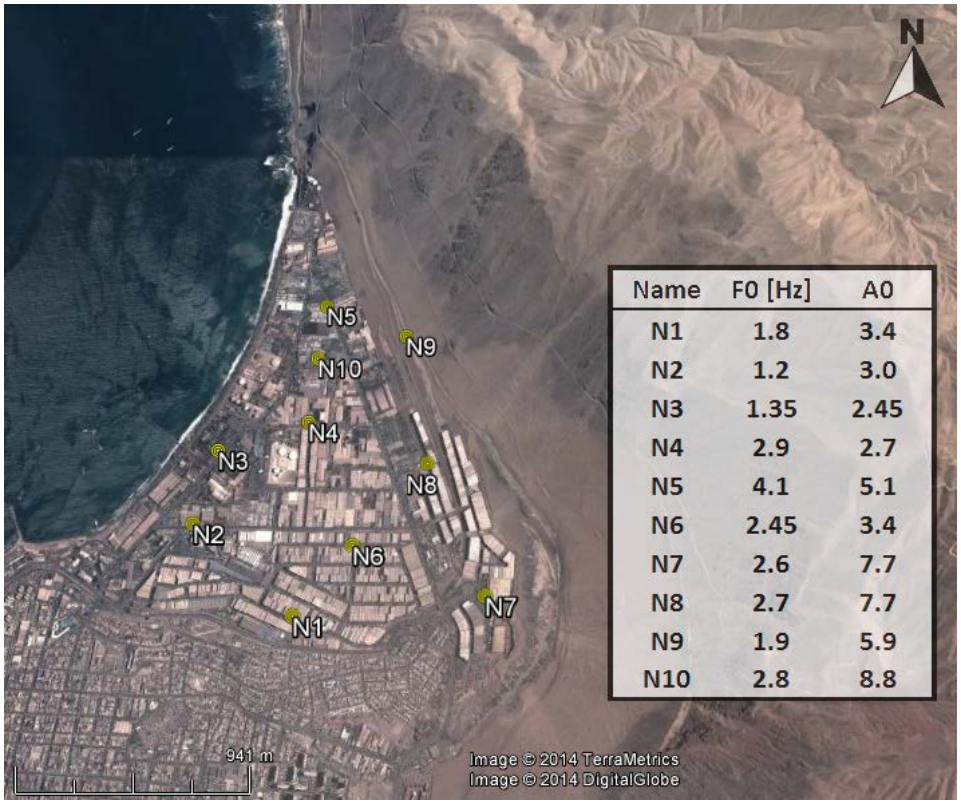

Name	F0 [Hz]	A0
N1	1.8	3.4
N2	1.2	3.0
N3	1.35	2.45
N4	2.9	2.7
N5	4.1	5.1
N6	2.45	3.4
N7	2.6	7.7
N8	2.7	7.7
N9	1.9	5.9
N10	2.8	8.8

Fig. 5.9 Typical Nakamura results in the ZOFRI area

5.3 Alto Hospicio city

Alto Hospicio is characterized by rigid gravels with a matrix of halite (commonly known as rock salt) (Marquardt et al., 2008). Most of the damage in this area was concentrated in masonry houses of up to 2 stories near the center of the city (Fig. 5.10). It is possible that partial dissolution of soil salts may have generated unstable areas (cavities) that were activated during the earthquake, since near the houses several cavities were identified in the surface (Fig. 5.12) as well as seismic induced cracks on the pavement.

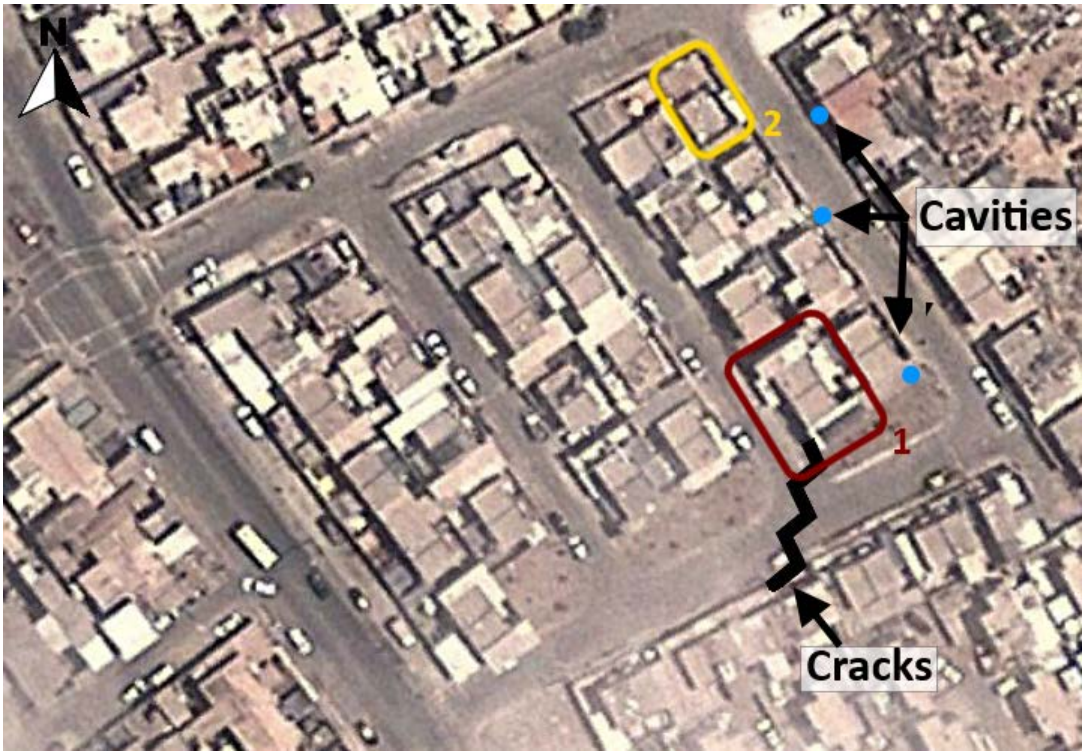

Fig. 5.10 Cases of study in Alto Hospicio. The black line represents the seismic induced crack in the pavement, while blue dots are the places where cavities were found

Fig. 5.11. Observed damage for case 2 of Fig. 5.9.

Fig. 5.12. (left) Observed damage for case 1 in Fig. 5.9 and (right) cavities in Alto Hospicio

5.4 Dunas I

"Dunas I" is a group of apartment buildings located to the south-east of Iquique (Figure 5). The seismic microzoning in Iquique characterizes this area as deposits of eolian sands of varied thickness (Becerra et al., 2014). The buildings are made of confined masonry and their height goes up to 4 stories. There are 2 types of structures, type A and type B as illustrated in Fig. 5.13 The only structural difference between them is the length. However, structural damage was seen only in buildings type A (Fig. 5.14).

A portable triaxial seismograph was placed on the top floor of each structure making it possible to estimate their post-seismic fundamental frequencies in the X and Y direction (Fig. 5.13) using the maximum amplitude of the Fourier spectrum.

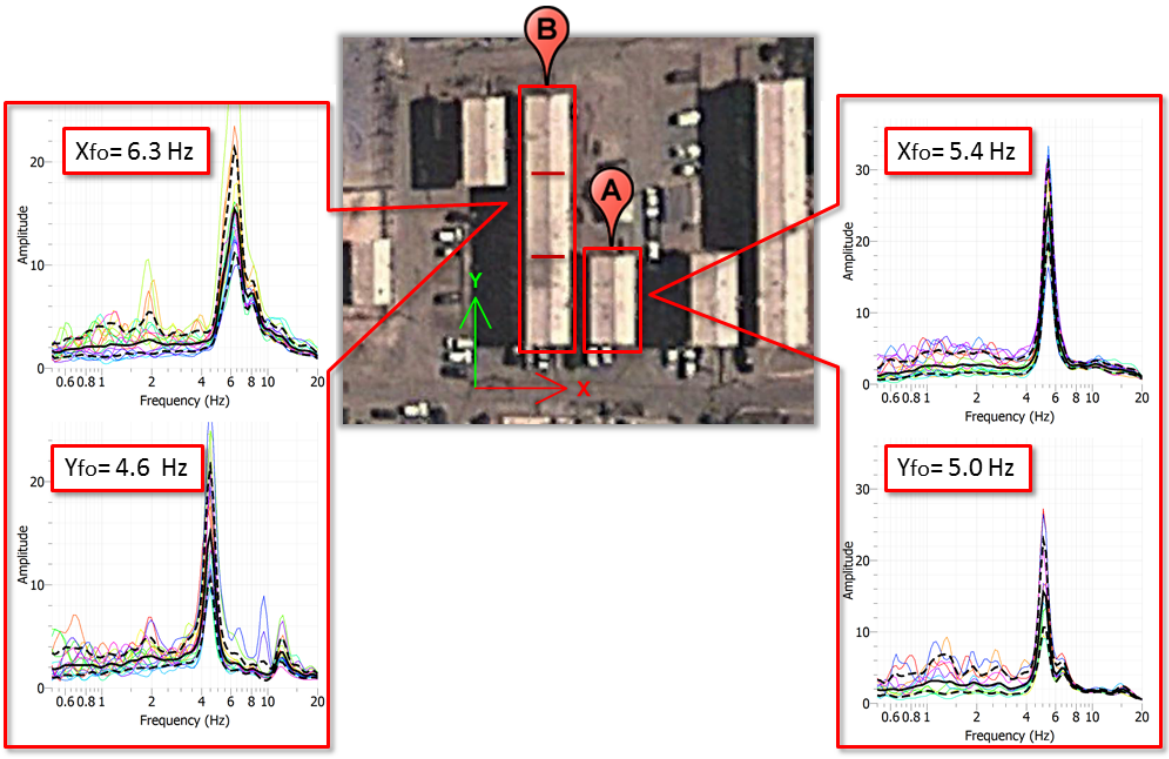

Fig. 5.13. Estimation of fundamental frequencies of buildings type A and B.

Furthermore, Nakamura's technique (Nakamura, 1989) was used on the sites to obtain the predominant frequency of the soil, as is depicted in Fig. 5.15. Note that, for the building A, the

post-seismic fundamental frequency is almost identical to the predominant soil frequency. Therefore, it is possible that damage of type A was controlled by resonance between the soil and the structure. However, further studies such as synchronized recording should be performed in order to confirm this hypothesis.

Fig. 5.14. Observed damage in buildings type A

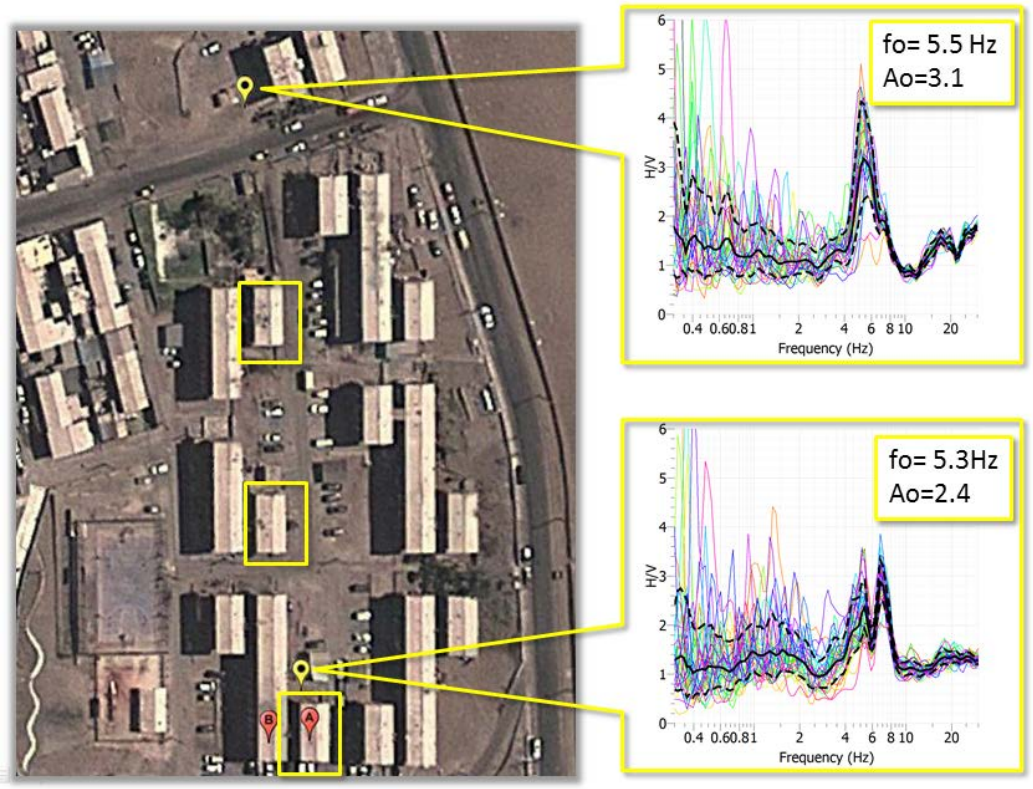

Fig. 5.15. Predominant frequencies in Dunas I obtained by Nakamura's technique. The buildings marked in yellow are the ones who suffered most structural damage.

5.5 References

Becerra, A., Podestá, L., Monetta, R., Sáez, E., Leyton, F., and Yañez, G. (2014). Seismic microzoning of Arica and Iquique, Chile. Manuscript submitted for publication.

Becerra, A. Seismic microzoning of Arica and Iquique, Chile (2014). Pontificia Universidad Católica de Chile.

Marquardt, C., Marinovic, N. and Muñoz, V. (2008). Geología de las ciudades de Iquique y Alto Hospicio, Región de Tarapacá, Carta Geológica de Chile, Serie Geología Básica, 113, 33.

Nakamura, Y. (1989). A method for dynamic characteristics estimation of subsurface using microtremor on the ground surface, Q.R. Rail. Tech, 25–30.

Centro Sismológico Nacional de la Universidad de Chile (CSN). http://www.sismologia.cl/

6. Slope Stability and Landslides

Natural slope failures along the coastal bluffs and interior creeks were observed throughout the region affected by the ground motion, from Arica in the north to Calama in the south. In most cases, however, they caused no damage to engineered systems. Several cases of rocks falling and raveling failures developed on cut slopes of route 1, route 5, and interior roadways, blocking traffic temporarily. No significant damage was observed on steep slopes stabilized with wire meshes and shotcrete. A deep-seated slope failure affected route A-16 between the cities of Iquique and Alto Hospicio, which is a critical road for the regional commerce. This failure delayed the emergency response operations and caused major traffic congestions in the days following the earthquake.

6.1 Slope Failures along Route A-16

On Route A-16 between Iquique and Alto Hospcio, a deep-seated slope failure occurred 2.5 km south of the *El Pampino* roundabout. The failure extended over 400 m on the west lane, with the largest displacements concentrated on a 100 m section as shown in Fig. 6.1. Vertical offsets of 20 cm – 40 cm and horizontal displacements of 10 cm – 30 cm were measured at the cut slope head, as seen in Fig. 6.2, and the estimated volume of displaced soil was approximately 3000 m^3.

This failure on route A-16 is located on the steep cliffs of Iquique, at an elevation of 215 m AMSL. The slope runs north-south, dips west at an angle of 24°, and is made primarily of marine sands underlain by Tertiary sedimentary rocks. The depth to bedrock is about 10 m – 15 m and the estimated peak ground accelerations for the main shock were 0.3g-0.4g.

Following the earthquake, traffic was permanently closed on the west lanes. The east lanes opened for emergency operations within a day and for regular traffic within three days. Shallow failures occurred at different locations on Route A-16, but they concentrated at higher elevations, near Alto Hospicio, as shown in Fig. 6.4. Rock falls on the hillside were pervasive, but the fallen material was removed rapidly to allow traffic to go through (Fig. 6.5, 6.6, 6.7). While raveling failures of non-stabilized slopes occurred repeatedly, road cuts protected with shotcrete and wire mesh performed well and only minor damages were observed. An example of a shotcrete lined slope on the hillside of Route A-16 is shown in Fig. 6.8. In addition, mechanically stabilized earth (MSE) retaining walls along some sections of the roadway performed well without any apparent distress as shown in Fig. 6.9.

6.2 Shallow failures

Shallow slope failures were of common occurrence on natural and cut slopes. On a private road in the Zofri area, a shallow slope failure induced settlements and cracks on the pavement as seen in Fig. 6.10. The slopes on either side of the road dip 30° SW and are made of marine eolian

sands and slightly cemented clumps. The depth to bedrock is approximately 25 m. The seismic displacements were small and in good agreement with the ground motion intensity at the site. Measured horizontal and vertical displacements were less than 10 cm, and the buildings on the slope crown showed no evidence of differential settlements.

Rock falls and mass waste in interior roadways

Rock falls and raveling failures of disaggregated material were spread throughout cut slopes in the Regions of Tarapacá and Antofagasta. In most cases, the fallen soil and rock fragments were plowed off the roads within a few days after the earthquake and the traffic flow was restored. A preliminary damage assessment on roads provided by MOP shows the extent of the damage as outlined in Table I.

The magnitude of the failures was in direct proportion to the slope angle, the looseness of the slope material and the site-to-source distance. For example, slopes of sedimentary rock on route A-16 (96 km from the epicenter) were significantly damaged, whereas steep loose-gravel slopes on Route 565 located 130 km from the epicenter, experienced only minor rock falls, as seen in Fig. 6.11 and 6.12.

Table I – Immediate damage assessment of roads issued by MOP on April 10^{th}

Location	Rock fall and mass waste scale	Traffic Allowed
Route 5 - km 2009-2023	Large	Yes
Route 5 - km 1970-1979	Large	Yes
Route 11-CH - km 36-77	Small	Yes
Route A-27 - km 41-51	Large	Yes
Route A-31 - km 70-71	Medium	Yes
Route A-31 - km 150-162	Medium	Yes
Route A-35 - km 40-70	Large	Yes
Route A-315 - km 0-11	Medium	Yes
Route A-23 - km 38	Large	No
Route A-345 - km 10-74	Large	Yes
Route A-331 - km 4	Large	Yes
Route A-307 - km 0-10	Large	Yes

Fig. 6.1 Deep seated slope failure on Route A-16 (-20.243028°, -70.124056°).

Fig. 6.2 Measured displacements of 40 cm (vertical) and 30 cm (horizontal) on the slope displacement of Route A-16. (-20.243028°, -70.124056°).

Fig. 6.3 Minor slope displacements and surface craks extending 300 m past the principal slope displacement on Route A-16. (- 20.243028°, -70124056°).

Fig. 6.4 Shallow slope failure on Route A-16 (-20.270436°, -70.111544°)

Fig. 6.5 Raveling failure on non-stabilized slopes overtopping the guardrails in Route A-16. (-20.249944°, -70.117747°)

Fig. 6.6. Disaggregated rock slides on Route A-16 (-20.264989°, -70.112106°)

Fig. 6.7. Disaggregated rock slides on Route A-16 (Photo courtesy of prensalibre.com)

Fig. 6.8. Undamaged steep cuts stabilized with wire mesh and shotcrete (-20.263819°, -70.112042°)

Fig. 6.9. Undamaged Mechanically Stabilized Earth (MSE) retaining walls adjacent to steep slopes (-20.251279°, -70.116173°)

Fig. 6.10. Slope displacement on the Zofri area. (-20.204153°, -70.130669°)

Fig. 6.11. Rock falls along Route A565, unimpeded traffic. (-19.942006°, -69.533139°)

Fig. 6.12 Damage on shoulders of Route A-555 induced by rock falls along unimpeded traffic. (-19.884222°, -69.468258°)